Dust Emission Modeling Using a New High-Resolution Dust Source Function in WRF-Chem With Implications for Air Quality

Sagar P. Parajuli[1] [iD], Georgiy L. Stenchikov[1] [iD], Alexander Ukhov[1] [iD], and Hyunglok Kim[2] [iD]

[1]Division of Physical Sciences and Engineering, King Abdullah University of Science and Technology, Thuwal, Saudi Arabia, [2]Department of Engineering Systems and Environment, University of South Virginia, Charlottesville, VA, USA

Abstract Air-borne dust affects all aspects of human life. The sources of dust have high spatial variation and a better quantification of dust emission helps to identify remediation measures. Orographic and statistical source functions allow a better estimation of dust emission fluxes in coarse-scale modeling, but a high-resolution source function is necessary to represent the highly heterogeneous nature of dust sources at the finer scale. Here we use a newly developed high-resolution (~500 m) source function in Weather Research and Forecasting model, coupled with chemistry (WRF-Chem) to simulate dust emission over the Middle East and North Africa and evaluate our simulated results against observations. Using a 4-km grid spacing, we also simulate the emission and transport of dust originating from the Tigris-Euphrates basin, one of the most important regional dust sources, and quantify the effects of this source on the air quality of the entire Arabian Peninsula. Results show that the use of new source function effectively represents the key dust sources and provides reasonable estimates of dust optical depth and concentrations. We find that the atmospheric dust originating from the Tigris-Euphrates basin alone exceeds the particulate matter 10 air quality standards in several downwind cities. Our results have broader environmental implications and indicate that the mobilization of depleted uranium deposited in Kuwait and Southern Iraq during the Gulf War (1991) could potentially affect the urban centers over the peninsula, albeit in low concentrations. Our results suggest that an integrated and coordinated management of the Tigris-Euphrates basin is necessary to maintain good air quality across the Arabian Peninsula.

1. Introduction

Dust emission is a complex process governed by several land-atmosphere interactions. Over the past three decades, dust emission models have benefited tremendously, from the rapid growth of high-resolution satellite and ground-based observations, advances in model physics, and the development of computational capability. However, several sources of uncertainty still exist in all commonly used dust models (Evan et al., 2014; Klose et al., 2014; Shao et al., 2011). One such source of uncertainty is the dust source function, commonly called erodibility, which is used to represent the spatial distribution of dust sources in global/regional dust models.

An accurate representation of the sediment content (or sediment supply), at a specific location, is a precondition for accurately modeling the dust cycle, including dust emission. It is widely accepted that the use of a dust source function improves the estimation of dust emission fluxes in global/regional models (Ginoux et al., 2001; Schepanski et al., 2009; Zender, Newman, & Torres, 2003). However, some recent studies show that the use of a dust source function is not necessary in certain regions (Parajuli, Yang, & Lawrence, 2016; Zender, Newman, & Torres, 2003), and that its use can be avoided by using a more accurate parameterization of the threshold friction velocity (Kok et al., 2014; Wu et al., 2016). Several source functions are currently in use in different models. Some of them are based on orography or elevation (e.g., Ginoux et al., 2001; Koven & Fung, 2008; Zender, Newman, & Torres, 2003), whereas others are based on observations and their statistics (e.g., Anisimov et al., 2017; Ginoux et al., 2012; Grini et al., 2005; Parajuli et al., 2014; Parajuli, Yang, & Lawrence, 2016; Schepanski et al., 2007). Most of these source functions work well in coarse-scale modeling; however, a high-resolution source function is necessary to resolve fine-scale processes affecting dust source mobilization (e.g., Anisimov et al., 2017). Parajuli & Zender, 2017 proposed a high-resolution dust source function based on sediment supply (hereinafter SSM source function), which they developed by combining a hydrologic upstream catchment area with Moderate Resolution Imaging Spectroradiometer (MODIS)

Writing - original draft: Sagar P. Parajuli
Writing – review & editing: Georgiy L. Stenchikov, Alexander Ukhov

reflectance data. Since this SSM source function uses both hydrological information and surface reflectance, it is expected to better represent dust sources such as playa/sabkha, sand dunes, and agricultural areas, which may not be captured by the commonly used elevation-based erodibility maps. Although a preliminary evaluation has been conducted using geomorphological data, this new source function has not been tested in global/regional dust models.

The Tigris-Euphrates river basin is one of the key dust source regions in the Middle East (Basart et al., 2016; Parajuli et al., 2014; Reid et al., 2008), with the highest intensity of dust emission in the region (Kontos et al., 2018; Prakash et al., 2015). Alluvial deposits and playa/sabkhas (Prospero et al., 2002) primarily characterize this area, which is heavily disturbed by anthropogenic activities such as urbanization and agriculture (Parajuli & Zender, 2017). This area is of prime importance for dust-related studies for several reasons. First, prevailing Shamal winds frequently transport dust from this area to the downwind region as far as Yemen and Oman affecting the air quality of the entire region. This results in increased atmospheric dust concentrations, such as during dust storms, which can cause severe respiratory health problems (e.g., Jiménez et al., 2010; Sajani et al., 2011). It is, therefore, important to understand the spatio-temporal variability of surface particulate matter (PM) concentrations and their origin. Second, depleted uranium (DU), which was exposed in the Tigris-Euphrates region during the Gulf War (1991), can be resuspended during large-scale dust storms and transported downwind; this constitutes a health hazard, especially when the suspended dust concentrations are high (Bou-Rabee et al., 1995). DU is a by-product of the uranium enrichment process and is commonly used in weapons because of its high density and low relative cost (McDiarmid et al., 2000). During the Gulf War, large amounts of DUs were dropped in the form of tank-fired shells and aircraft rounds in Kuwait and Southern Iraq (Bem & Bou-Rabee, 2004; US Army Environmental Policy Institute, 1995). We are not aware of any previous study in the literature that directly considered the potential dispersion of DU particles by aeolian transport. Previous studies have considered the transport of environmental pollutants, several kilometers downwind from the source regions, such as the downwind transport of evaporite salts from the Makgadikgadi Depression in Botswana (Wood et al., 2010). Therefore, it is important to investigate the spatio-temporal dynamics of pollutants transported from the Tigris-Euphrates region and to determine how much these pollutants affect the air quality in downwind regions. To cover all these aspects, we implement a newly developed high-resolution (~500×500m) SSM source function in the Weather Research and Forecasting model, coupled with chemistry (WRF-Chem), in order to simulate dust emissions and the resulting surface PM concentrations over the Middle East and North Africa (MENA). We aim to answer the following research questions:

1. How does a high-resolution dust source function perform in a regional climate model and how does it improve the representation of dust emission fluxes in the model?
2. What is the best way of tuning the model so that all parameters of dust, including dust optical depth, dust concentrations, and size distributions, are consistent with observations?
3. How does the dust emitted from the Tigris-Euphrates basin affect the dust abundance in downwind regions and what is the contribution of the Tigris-Euphrates dust sources on the total dust distribution over the Arabian Peninsula?

This paper is organized as follows. We present a description of observational datasets and our methods in section two, where we discuss the WRF-Chem model settings, model experiments, and the specifics of model tuning in that order. In section 3, we present the results. More specifically, we attempt to answer the first research question listed above in section 3.1. In section 3.2, we evaluate our model results against observations and focus on the second research question. In section 3.3, we investigate the third question in detail. Our conclusions are presented in section 4 in which we also present the broader impacts of our research with a further discussion of the results.

2. Data and Methods

2.1. Observations

To test and calibrate the model runs, we use a number of datasets to obtain key dust parameters, including the aerosol optical depth (AOD), the dust optical depth (DOD), the Angstrom exponent (AE), and the dust concentrations for the simulation period, which is the entire year of 2015.
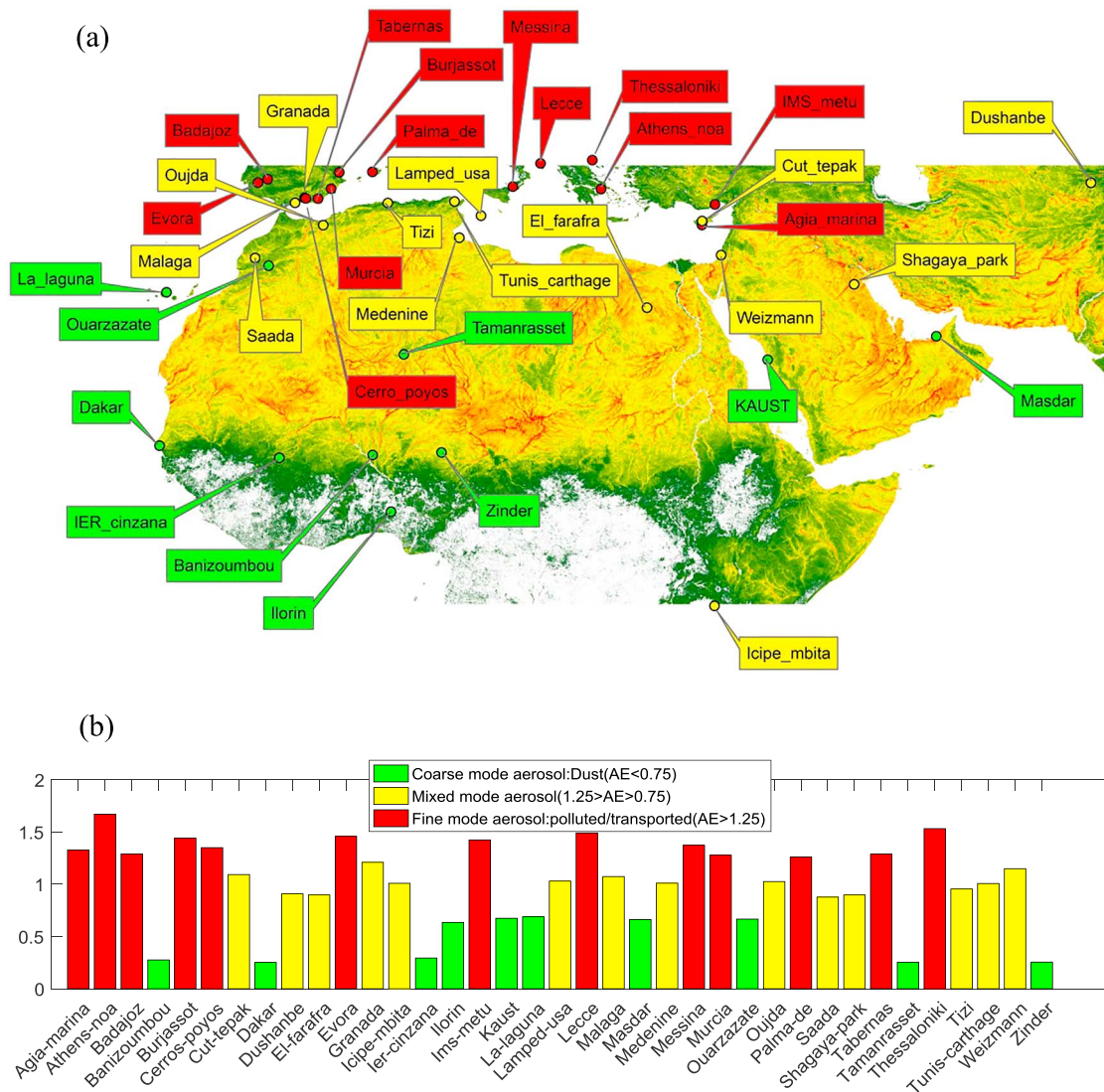
Figure 1. (a) Spatial distribution of 37 Aerosol Robotic Network (AERONET) stations used in this study. Basemap shows the SSM source function reproduced from Parajuli and Parajuli and Zender (2017), in which red and green mean higher and lower sediment supplies, respectively. (b) Average Angstrom exponent values (average of 2015) for different stations. Stations in both figures are colored green, yellow, and red to indicate the dominance of coarse mode, mixed mode, and fine mode aerosols, respectively.

We use aerosol data retrieved from Cloud-Aerosol Lidar with Orthogonal Polarization (CALIOP) onboard Cloud-Aerosol Lidar and Infrared Pathfinder Satellite Observations (CALIPSO), known to generate 3-D quantitative characterizations of aerosols and cloud globally with unprecedented vertical details. We use CALIOP level-3 day/night aerosol profile products (AOD and DOD), which are monthly aerosol products generated by aggregating version 3 level-2 monthly statistics at 2°(lat)×5°(lon) resolution, extending up to 12-km height (Winker et al., 2013).

We also collect AOD and AE data from AERONET stations (Holben et al., 1998) over the entire study area. We select a total of 37 stations with, at least, 4 months of data available in 2015 (Figure 1a). We use a cloud-screened and quality-assured level 2.0 version of directly measured AOD values (direct sun algorithm). Because the AOD values are not available at our desired wavelength of 0.550 μm, we derive the AOD, at this wavelength, using the commonly used technique based on AE values (e.g., Prakash et al., 2015):

$$AOD(0.550) = AOD(0.675) \times \left(\frac{0.550}{0.675}\right)^{-\alpha} \tag{1}$$

where α is the AE defined as

$$\alpha = \ln\frac{AOD(0.440)}{AOD(0.675)} \Big/ \ln\frac{0.675}{0.440} \tag{2}$$

Figure 1b shows the average Angstrom exponent values, at each Aerosol Robotic Network (AERONET) station, for 2015. Green indicates stations that have an average AE less than 0.75, meaning that these stations are more representative of localized, coarse-mode dust. Most stations located in Sahel and the desert strip of the MENA region are in this category. Stations in red exhibit an AE greater than 1.25, indicating that these stations are highly affected by fine-mode aerosols such as transported fine dust, anthropogenic pollution, or biomass burning aerosols. Most of the stations in the northern part of the study domain fall in this category; these stations are either located close to industrial cities, or affected by transported dust. The stations in yellow indicate the presence of both coarse and fine mode aerosols.

From AERONET, we also use an aerosol number density and a particle size distribution (PSD) obtained by an inversion algorithm (Dubovik & King 2000). The AERONET concentrations and PSD represent the average properties of the entire atmospheric column. We use the AERONET V3, level 2.0 product (Dubovik et al., 2000) that provides an aerosol volume concentration in 22 bins, with a radius between 0.05 and 15 μm. (https://aeronet.gsfc.nasa.gov/new_web/Documents/Inversion_products_V2.pdf). Note that in our model, the simulated PSD ranges between 0 and 10 μm only. We obtain these data from 15 AERONET stations for which data are available for all months of 2015.

We also use MODIS level-2 Deep Blue AOD data (Hsu et al., 2004), which are available daily, for the whole globe, at a resolution of ~0.1° × 0.1°. We use the latest version of the MODIS dataset (collection 6; Hsu et al., 2013) because of its extended coverage and improved Deep Blue aerosol retrieval, compared to its earlier version (collection 5). We process AOD data of both Terra and Aqua satellites on a daily basis and use the average of two data for analysis.

AE criterion is commonly used to extract the coarse-mode component from AOD data, as it is believed to represent "dust" only (Eck et al., 1999; Ginoux et al., 2012; Parajuli & Zender, 2017). However, in our case, using this criterion is not effective as the coarse-mode AOD from MODIS and AERONET is significantly higher than the Modern-Era Retrospective Analysis for Research and Applications (MERRA) DOD (Figure S1 in the supporting information). Use of this criterion also reduces the number of available observations, which is also why we opt not to use it, but instead compare our DOD results directly with AOD, using MODIS and AERONET data. As a quality control measure, we choose only the AERONET stations and MODIS grid cells for which at least 7 days of data are available in each season. We categorize the seasons as winter (December–February), spring (March–May), summer (June–August), and fall (September–November).

We also use the MERRA version 2 data (Rinecker et al., 2011) for comparison. Aerosol data from MERRA-2 dataset assimilate several satellite observations, including MODIS AOD (Gelaro et al., 2017). We specifically use tavg1_2d_aer_Nx and inst3_3d_aer_Nv products for getting 2-D AOD/DOD data and 3-D PM10 (PM with diameter <10 μm) concentrations, respectively. Note that although MERRA DOD corresponds to "dust" only, it is a model product obtained by assuming a fixed contribution of dust on total aerosols, and thus, the DOD may not be realistic.

2.2. WRF-Chem Model Setup

In this study, we use the WRF-Chem version 3.8.1. To calculate the dust emission, we use one of the most commonly used dust schemes available in WRF-Chem, developed by U.S. Air Force Weather Agency (AFWA). The AFWA dust scheme follows the Global Ozone Chemistry Aerosol Radiation and Transport (GOCART) dust emission (Ginoux et al., 2001) scheme, which is modified to account for saltation and is therefore more suitable for high-resolution simulations (Jones et al., 2011). The AFWA dust scheme considers key factors governing dust emissions, as parameterized by Marticorena and Bergametti (1995), which is described in adequate detail by LeGrand et al. (2019). Further descriptions and evaluations of AFWA can be

Table 1
Physics and Chemistry Options for the WRF-Chem Model Used in This Study

Description		Namelist options	References
Physics	Microphysics	mp_physics = 2	Lin et al. scheme
	PBL scheme	bl_pbl_physics = 2	MYJ (Janjic, 1994)
	Surface layer physics	sf_sfclay_physics = 2	Monin-Obukhov (Janjic Eta)
	Land Surface Model	sf_surface_physics = 2	Unified Noah land surface model (Chen & Dudhia, 2001)
	Convective parameterization	cu_physics = 3	Grell-Freitas (Grell & Freitas, 2014)
	Radiative transfer model	ra_lw_physics = 4, ra_sw_physics = 4	Rapid radiative transfer model (RRTMG; Iacono et al., 2008)
Chemistry	Chemistry option	chem_opt = 301	GOCART coupled with RACM
	Dust scheme	dust_opt = 3	GOCART with AFWA modifications (Jones et al., 2011)

found in Su and Fung (2015) and Cremades et al. (2017). Briefly, the horizontal saltation flux (Q) is first calculated, according to the equation given by White (1979), and is defined as follows:

$$Q = \begin{cases} \frac{\rho_a}{g} u_*^3 \left(1 + \frac{u_{*t}}{u_*}\right)\left(1 - \frac{u_{*t}^2}{u_*^2}\right), & u_* > u_{*t} \\ 0, & u_* < u_{*t} \end{cases} \tag{3}$$

where ρ_a is the air density, g is the gravitational acceleration, u_* is the friction velocity, and u_{*t} is threshold friction velocity, which mainly depends on particle size, particle density, and soil moisture.

Q is then converted into a vertical mass of dust flux (F_{bulk}), using the following equation:

$$F_{bulk} = C \times S \times \alpha \times Q \tag{4}$$

where C is usually used as a tuning factor, S is a spatially varying dust source factor commonly known as *erodibility* (replaced with the SSM source function in this study), and α is the sandblasting mass efficiency calculated as a function of clay content.

The vertical mass flux of dust, F_{bulk}, is subsequently distributed into five dust emission bins, with radii ranges of 0.1–1.0, 1.0–1.8, 1.8–3.0, 3.0–6.0, and 6.0–10.0 µm, and with respective mass fractions of 10.74, 10.12, 20.78, 48.17, and 10.10%.

The physics and chemistry model settings are given in Table 1. Because our focus is on dust emissions, we "turn-off" the emission of all other pollutant species. For this reason, the model-simulated AOD is called "DOD" hereinafter. We do not apply chemical/aerosol boundary conditions, and emissions of biomass burning, sea-salt, and anthropogenic aerosols are turned off. We allow the aerosol-radiation feedback but do not include the indirect effect of the aerosol. We use the 21-category MODIS and 30-arc-second U.S. Geological Survey GMTED2010 data for specifying the land-use categories and orography, respectively, which are the default options in the WRF starting version 3.8.

Most dust events in the region are associated with Shamal winds (e.g., Francis et al., 2017), synoptic cold fronts (e.g., Vishkaee et al., 2012), and haboobs (Anisimov et al., 2018; Khan et al., 2015), all of which cause high wind speeds and dust emissions. Therefore, the use of accurate meteorological boundary conditions is important to capture these regional weather features. Considering our high-resolution simulations, initial and lateral boundary conditions are provided using high-resolution ECMWF operational analysis data downloaded at F640 Gaussian grids (~15 km) and are available every 6 hours. The sea surface temperature (SST) values are also updated in our simulations, using the same ECMWF dataset.

2.3. Domains and Experimental Settings

In this study, two domains are defined, as shown in Figure 2: (1) a 12-km spatial resolution coarser domain that covers the entire MENA region and (2) a finer, 4-km spatial resolution domain covering the Arabian Peninsula.

We conduct our simulations by season for the entire year of 2015. For each season, simulations are started 1 week before and results of the first week are discarded as spin-up. In order to address our research questions
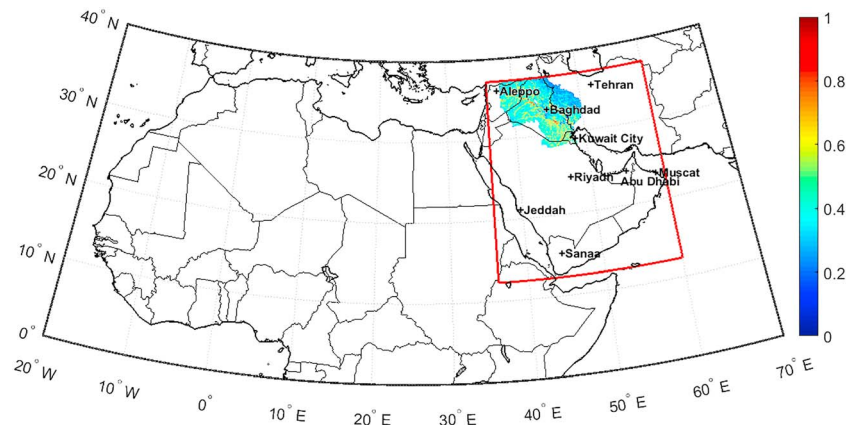
Figure 2. Outer (black) and inner study domains (red) covering Middle East and North Africa (MENA) and the Arabian Peninsula, respectively. The Tigris-Euphrates dust source region is outlined by the SSM source function values that range from zero to one.

defined in section one, we conduct simulations in two parts as presented in Table 2. In the first part, we conduct simulations in the parent domain, over the entire MENA region using a 12-km grid spacing and evaluate the results against a set of observational and reanalysis data. We conduct two experiments using two different source functions: (1) the new high-resolution dust source function developed by Parajuli and Zender (Parajuli & Zender, 2017) and (2) the existing source function available in WRF-Chem by default, commonly known as "topographic source function" (Ginoux et al., 2001).

In the second part, we conduct simulations using 4-km grid spacing in order to study the emission and transport of dust over the Arabian Peninsula. Although our region of interest is the Arabian Peninsula, it is important to incorporate all dust sources of the MENA region in order to obtain a realistic simulation of the dust loading over our study region. Past studies show that significant dust exchange occurs between North Africa and the Arabian Peninsula, across the Gulf of Aden and Red Sea (e.g., Prakash et al., 2015). Therefore, we nest the 4-km inner domain of the Arabian Peninsula within the 12-km outer domain using a two-way feedback. In order to quantify the contribution of Tigris-Euphrates dust sources on total dust loading, we run two experiments. In the first experiment, only the Tigris-Euphrates basin is allowed to emit dust, using the SSM source function, in both the inner and outer domains. The outline of the Tigris-Euphrates basin is derived by combining the hydrologic boundaries of the basins obtained from the HydroBASINS database (Lehner & Grill, 2013), in particular using hybas_eu_lev04_v1c data. For calculating dust emissions, the erodibility factors are assigned different values: SSM source function values for the grids lying within the Tigris-Euphrates basin and zero values for the remaining domains. Figure 2 shows the region of the Tigris-Euphrates basin, together with the source function values. In the second experiment, we allow the dust emission from the entire MENA region by using the SSM source function, in both the inner and outer domains. We then define the Tigris-Euphrates contribution as the ratio of dust emission in the first and second experiments.

Table 2
Description of Experiments and Their Objectives

Part	WRF-Chem domains	Nesting	Spatial res. (km)	Source function	Experiments	Objective
I	Middle East and North Africa (MENA; 0–40°N, 20°W–70°E)	No	12×12	SSM and topographic	1. SSM 2. Topographic	Evaluate dust source functions
II	Arabian Peninsula (AP; 12–37°N, 36–60°E)	Yes (inner domain nested within outer domain)	4x4	SSM only	1. Tigris-Euphrates (TE) sources 2. All dust sources	Calculate PM10/PM2.5 caused by TE sources and determine their contribution on total dust

Abbreviation: PM: particulate matter.

To investigate the effects of the dust sources of the Tigris-Euphrates on the air quality of our study region, we examine the model-simulated PM10 and PM2.5 values in the following nine highly populated cities of the Middle East: Tehran, Baghdad, Riyadh, Jeddah, Abu Dhabi, Kuwait City, Sanaa, Aleppo, and Muscat. We extract the model-simulated PM10 and PM2.5 values at the lowest model level from the grid cells containing those cities and compare them with the prevailing air quality standards. According to U.S. National Ambient Air Quality Standards, the 24-hr average PM10 concentration should not exceed 150 $\mu g/m^3$ more than once in a year (National Ambient Air Quality Standards, 2013); the standard for PM2.5 is 35 $\mu g/m^3$.

We conduct two preliminary experiments to evaluate the effects of nudging on the simulated DOD for the summer season of 2015, by applying grid nudging with a relatively strong nudging coefficient of 0.0006, based on recommendations from previous studies (e.g., Anisimov et al., 2018; Flaounas et al., 2016; Kumar et al., 2014). We perform the first experiment by applying nudging on u and v, excluding the PBL, and we conduct the second with nudging including the PBL (i.e., at all levels). By evaluating the simulated DOD against MODIS AOD, we find that the former was superior to the latter (see Figure S2). Therefore, we apply nudging (only above PBL) in all our simulations.

We use skill score (Taylor, 2001) for comparing the model simulations with the observations (e.g., Klingmüller et al., 2018). The skill score (S) is defined as:

$$S = \frac{4(1+r)^4}{\left(\frac{\sigma_1}{\sigma_2} + \frac{\sigma_2}{\sigma_1}\right)^2 (1+r_0)^4}$$

(5)

where r is the correlation coefficient, σ_1 and σ_2 are the standard deviations of model simulations and observations, respectively, and r_0 is the maximum attainable correlation.

The skill score values range from 0 to 1, and a higher value means a better match between the model and observations. We calculate the skill scores using both MODIS and AERONET AOD. In order to ensure the reliability of calculated skill scores, we calculate skill scores only in those grid cells (for MODIS) or stations (for AERONET) in which the calculated correlation coefficients (r) are significant ($P<0.2$).

2.4. Dust Emission Tuning

We determine the tuning coefficient C in equation ((2)) by calibrating the simulated DOD against CALIOP DOD, as done in several previous studies (e.g., Kalenderski et al., 2013; Prakash et al., 2015; Su & Fung, 2015; Zhao et al., 2010), but on seasonal basis. We decide to use CALIOP data for tuning considering the fact that it is the only observational dataset providing dust's optical depth. Although CALIOP has a 16-day repeat cycle at a particular location, it can still capture the larger features of a dust plume, from an adjacent swath, because the dust events in this region usually have large spatial coverage. Further, for tuning purpose, we use DOD values averaged over a large-region, and seasonally, which reduces the effect of undersampling.

Using the tuning factor, we change emissions uniformly over the domain to match the simulated area-averaged DOD with that from the CALIOP observations. In the first part, we use the average DOD from the outer domain, and in the second part (nested simulations), we use the average DOD from the inner domain. The averaged DOD values for each area, obtained from the CALIOP data used for tuning, are presented in Table 3. Tuning coefficients are calculated for both source functions in the first part as presented in Table 3. In the second part, they are calculated for the SSM source function only.

In the second part (with nesting), we initially intended to use the same tuning coefficients to those obtained in the first part (nonnesting case) for the SSM source function. However, use of those coefficients is not appropriate because the simulated DOD (averaged over the inner domain) differs significantly with the observed DOD; this requires us to adjust the magnitude of the tuning coefficients further. This is partly because of the dust exchange between the outer and inner domains and partly because of the higher spatial resolution of the inner domain (4 km) in the nesting case. Adjusting the coefficient for the inner domain only to match the observed DOD is difficult, even after changing the coefficient significantly. Therefore, we adjust the tuning coefficient for the outer domain as well. In this case, using two coefficients is not appropriate, as any combination of two coefficients can yield the desired DOD. To avoid this, and for consistency, we tune the model using the same coefficient in both domains. The final coefficients calculated in this manner are listed in Table 3.

Table 3
Target Dust Optical Depth (DOD) and Tuning Factors for Different Experiments

Part	Description	Averaged over	Target average DOD				Tuning coefficients			
			DJF	MAM	JJA	SON	DJF	MAM	JJA	SON
I	SSM source function	Middle East and North Africa	0.12	0.20	0.24	0.10	0.012	0.129	0.115	0.079
	Topographic source function						0.195	0.176	0.179	0.118
II	Nesting case-SSM only	Arabian Peninsula	0.12	0.29	0.41	0.18	0.136	0.196	0.120	0.110

Abbreviations: DJF, December–February; JJA, June–August; MAM, March–May; SON, September–November.

The tuning coefficients are different, depending on the season, as they are sensitive to the choice of source function. Tuning factors are higher for a topographic source function in all seasons than for a SSM source function, meaning that the SSM yields more dust in total compared with a topographic source function. The tuning coefficients are partially governed by the target optical depth used, which vary by seasons. Therefore, the coefficients are different in different seasons. The seasonal difference in tuning coefficient also arises because the factors controlling dust emissions, such as winds, soil moisture, vegetation, and agricultural activities, have strong seasonality. The model adjusts the dust emission intensity differently because two source functions have different dust emitting areas that interfere with the spatial patterns of controlling factors differently. For example, the SSM has fewer grid cells with a high emission intensity but has a larger area of dust generation than the topographic source function (see discussion in section 3.1). Therefore, the coefficients are different for the two source functions. The difference in magnitude of the tuning coefficient for the SSM, between the nesting and non-nesting cases, is largest in winter, which, possibly, indicates stronger feedback between parent and nested domains in winter while using the SSM.

2.4.1. Dust Size Distributions

It is important to ensure that the simulated PSDs are realistic because the aerosol optical properties (and therefore the tuning process) depend on them. Dust particles do not coagulate, and we do not account for the condensation of liquids on dust particles. Therefore, the size distribution of atmospheric dust mainly depends on the efficiency of the removal process of the size-dependent particles as well as the size distribution of emitted dust that is currently prescribed in the model. The AFWA dust emission scheme prescribes emitted dust in five bins with different fractions, as mentioned in section 2.2. In this study, we also change the size distribution of emitted dust so that the simulated dust PSDs are consistent with AERONET observations. Note that when we change the default size distribution of emitted dust, it then affects the simulated DOD, and thus the tuning. For example, when we increase (decrease) the clay fraction (first bin of the five bins, with 0.10- to 1.0−μm radius), it increases (decreases) the resulting DOD because finer particles are more effective in scattering per-unit mass than coarser particles in the visible bands. Therefore, the model has to be retuned to achieve the same optical depth, whenever the size fraction is changed.

To change the size fractions of the emitted dust in the model, we adjust the parameter "distr_dust" under the "phys/module_data_gocart_dust.F." We note that while implementing the new PSD, we also fix a bug in the WRF-Chem model, under the subroutine "optical_prep_gocart" in the fortran file module_"optical_averaging.F". Because of this bug, dust particles with radii smaller than 0.46 μm are not taken into account when calculating volume-averaged refractive index. Since finer particles contribute more significantly than coarser particles to the AOD per unit mass; the resulting AOD was underestimated previously. We note that this bug has been fixed in WRF-Chem v4.0.2.

Available observations show that the clay fraction of emitted dust is very small, approximately 4.4% (Kok, 2011). The AFWA dust scheme currently assumes 10.74% for this bin. Khan et al. (2015) reduced this fraction from 7 to 1%, in the GOCART dust scheme, and showed that the resulting PSD had a better match with the AERONET size distribution. In this study, we test three different scenarios with different clay fractions (Table S1 in the supporting information): a high fraction (38%), a medium (20%), and a small fraction (4%), based on a previous study by Kok (2011).

3. Results

We compare the dust source functions in section 3.1 and evaluate the overall model performance in section 3.2, focusing on the first and second research questions, respectively. For both of these analyses,
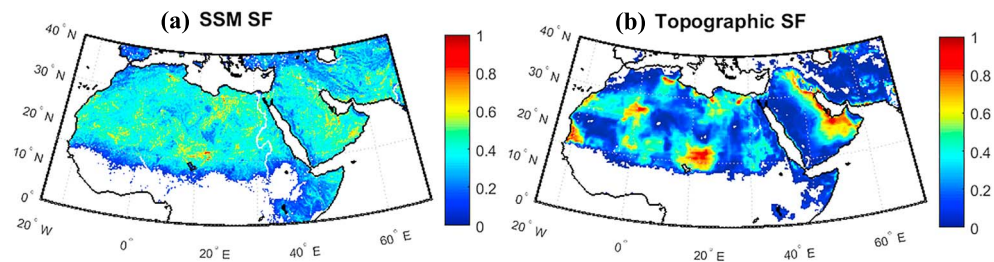
Figure 3. The two dust source functions used in this study: (a) the SSM source function developed by Parajuli and Zender (2017) and (b) the topographic source function developed by Ginoux et al. (2001).

we use results from the 12-km simulations (Part I), which cover the entire MENA region, except for comparison of PM10 and PM2.5, for which we use results from the high-resolution, 4-km simulations (Part II). We analyze the impact of Tigris-Euphrates dust sources in section 3.3, focusing on the third research question, in which we use the results from 4-km simulations that cover the Arabian Peninsula.

3.1. Comparison of Dust Source Functions

Figure 3 shows the SSM and the topographic source functions at a 12-km resolution. The topographic source function appears to be spatially more consolidated, with individual dust sources stronger than the SSM source function. However, the SSM source function has multiple finer-size source regions, with an intensity lower than the intensity in the topographic source function. We can see this, for example, over the northern part of the parent domain and over the Sahel region. Over the Arabian Peninsula, the topographic source function exhibits a strong east-west gradient that follows the topographic contours of the region, but this gradient is not present in the SSM source function. A study of the regional geomorphology shows that this area is characterized by a mixture of sabkhas, sand dunes, stony surfaces, and fluvial systems (Parajuli et al., 2014; Parajuli & Zender, 2017; Prospero et al., 2002), each of them having varying dust emission potentials. Therefore, it is unlikely that the erodibility would entirely follow the topography of this region. The SSM source function better represents the spatial variability of the dust sources in the regional scale.

The dust emission resulting from the use of two source functions depends on several factors. For example, the SSM source function has more grid cells as dust sources than the topographic source function. Consequently, the SSM source function produces a higher emission of dust in areas such as south of Sahel and the northern part of the domain, compared to the topographic source function. However, the SSM has fewer grid cells with a high emission intensity and are distributed more uniformly than in the topographic source function, as clearly seen in the emission histograms (Figure S3). In such hot spots, the topographic source function generates more dust. Although the emissions in particular locations may be different with the two source functions, the integral is tuned to achieve the same observed DOD, and in both cases we assume the clay emission to be 20% (section 2.4).

We note that the assumed size distribution of the emitted dust also affects the model-calculated dust emissions. For example, a larger fraction of clay particles will lower the dust emission, as shown in Figure S4. This can be explained by the fact that finer clay particles produce a higher optical depth per unit mass. Consequently, the model is forced to emit less dust to achieve the same observed DOD.

Figure 4 shows the simulated dust emission fluxes, using the SSM and the topographic source functions for different seasons. There are subtle differences in the emission distribution. For example, over the well-known Bodélé depression, the emission is generally higher and the emission areas appear larger with the topographic source function than with the SSM source function, which is more evident in the difference map (Figures 4i–4l). This is not surprising because the Bodélé sources appear much larger in the topographic source function than in the SSM source function (Figure 3). Note that the topographic source function was originally scaled using satellite-derived aerosol data from the Total Ozone Mapping Spectrometer (TOMS; Ginoux et al., 2001). Because satellite data measure the dispersed atmospheric dust, the Bodélé source region could appear larger in the topographic source function.

The Tigris-Euphrates region (~32°N, 48°E) appears to emit more dust when using a topographic source function than using a SSM source function. This is especially pronounced in summer (compare Figures 4c and
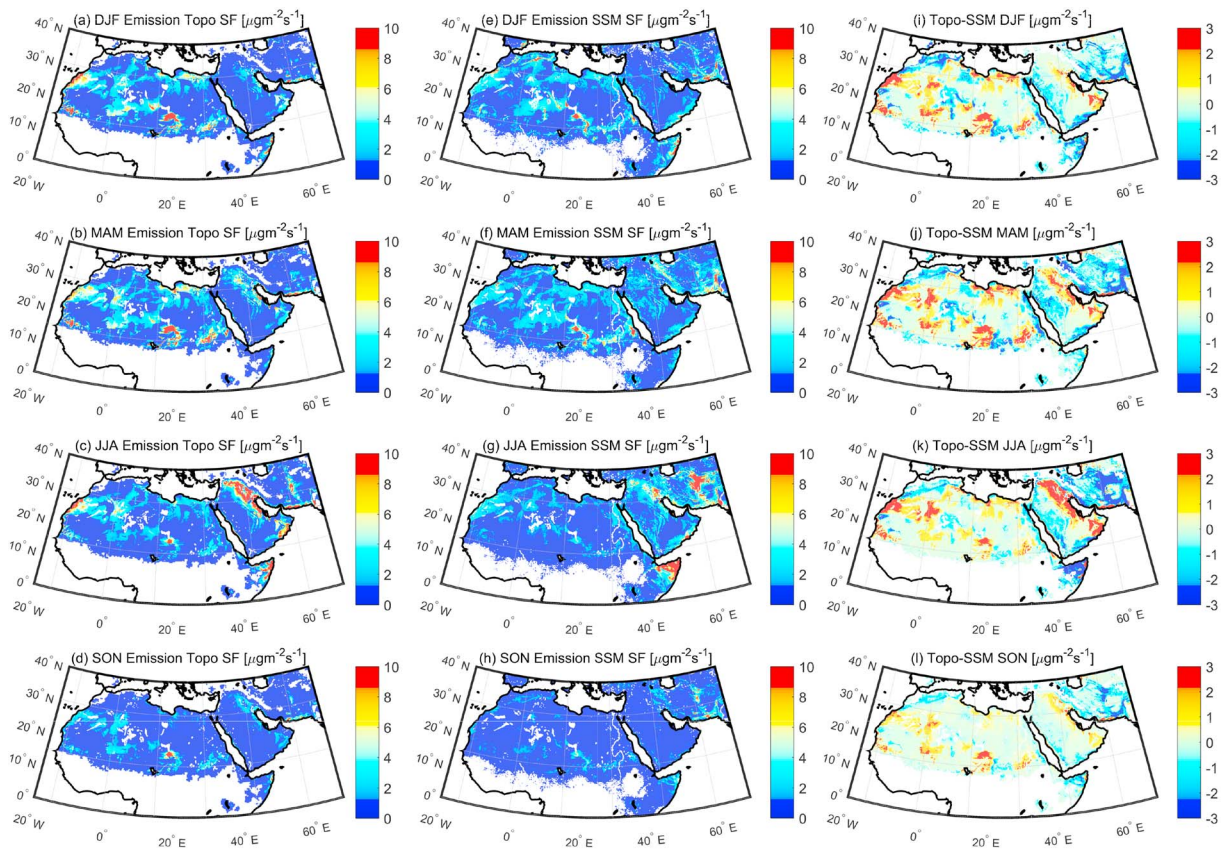
Figure 4. Model-simulated dust emission fluxes using the two source functions, and their differences, for all seasons of 2015. (a–d) A topographic source function, (e–h) a SSM source function, and (i–l) their differences.

4g). However, over the basins of Iran, Afghanistan, and Pakistan (~30°N, 60°E), SSM yields considerable dust emissions in all seasons from many more grid cells than the topographic source function (Figures 4i–4l). These regions are characterized by several small dry lakebeds consisting of playas (Parajuli & Zender, 2017; Prospero et al., 2002) that feed the frequent large-scale dust storms in the region (Rashki et al., 2015). The topographic source function shows low-to-no dust emissions in the western Arabian Peninsula. Numerous small playas and wadis characterize this region (Parajuli & Zender, 2017), which are correctly represented as dust sources in the SSM source function. Some previous studies also show significant dust emissions from this region (e.g., Anisimov et al., 2017).

The total annual dust emission budgets from the entire MENA region obtained using the two source functions for 2015 are presented in Table 4. The SSM source function yields higher dust emissions in all seasons compared to the topographic source function because additional finer-scale dust sources are identified by the SSM source function. Note that although the simulated domain-averaged DOD is the same in the two cases, the emissions are different because the relationship between emission and optical depth is not linear. The order of annual emissions seems reasonable since the order of modeled total annual global dust emission usually range from 1,500 to 2,000 Tg/year (e.g., Zender, Bian, & Newman, 2003). However, note that the total annual dust budget depends upon the DOD constraint applied for tuning; therefore, care must be exercised when comparing these values with other estimates. For example, we have noticed that using MODIS or AERONET AOD for tuning yields significantly higher emissions than using CALIOP DOD.

Figure 5 shows the DODs simulated using the two source functions as compared to MODIS AOD for four dustiest days, that is, the days with the highest daily mean AOD at KAUST station in each season. The spatial patterns of dust simulated by the model are consistent with the MODIS dataset. The Arabian Peninsula and northeast Africa appear particularly active on 28 April and 8 August 2015, which is consistent with the model and MODIS data. Despite the differences between the two source functions (Figure 3), we find that

Table 4
Total Dust Emission Budget (2015) From the Middle East and North Africa

	Total dust budget (Tg) from MENA (0–40°N, 20°W––70°E)	
Seasons	SSM source function	Topographic source function
DJF	184.5	160.5
MAM	214.1	191.3
JJA	242.1	211.5
SON	87.2	77.9
Total	727.9	641.3

Abbreviations: DJF, December–February; JJA, June–August; MAM, March–May; MENA: Middle East and North Africa; SON, September–November.

after a proper tuning at large scale, the DODs generated by the two source functions are quite similar (Figure 5, first and second columns). However, the SSM source function, as expected, generates more fine features of dust distribution and fits better for high-resolution simulations. Note that in the above simulation, we aggregate the original 0.5-km SSM source function to a 12-km grid spacing. The advantage of the SSM source function would be more significant when simulating dust emission on a finer grid. The key benefit of using the SSM source function is that it can represent regional, "point-scale" dust sources, whereas the existing coarse-scale source functions cannot. In the following sections, we obtained all the results using the SSM source function.

3.2. Model Performance

In this section, we apply the SSM source function in the model and evaluate the overall model performance against a set of observations discussed in section 2.1. All the results presented here are derived from the 12-km simulations covering the entire MENA region (Part I), except for the comparison of PM10 and PM2.5, in which we use results from 4-km simulations (Part II).

3.2.1. Dust Optical Depth

Figure 6 shows a comparison of the model- simulated DOD with all sets of observations used in this study. AERONET data represent the AOD averaged over all 37 stations. To be consistent, the model output, MERRA, MODIS, and CALIOP data are averaged over 37 grid cells containing the AERONET stations. The first three sets of bars show the seasonal average DOD. The simulated DODs are in very good agreement with both MERRA and CALIOP DODs, demonstrating that the model results are robust. The latter four sets of bars show the total AOD (not only dust) from MERRA, MODIS, AERONET, and CALIOP data. Total
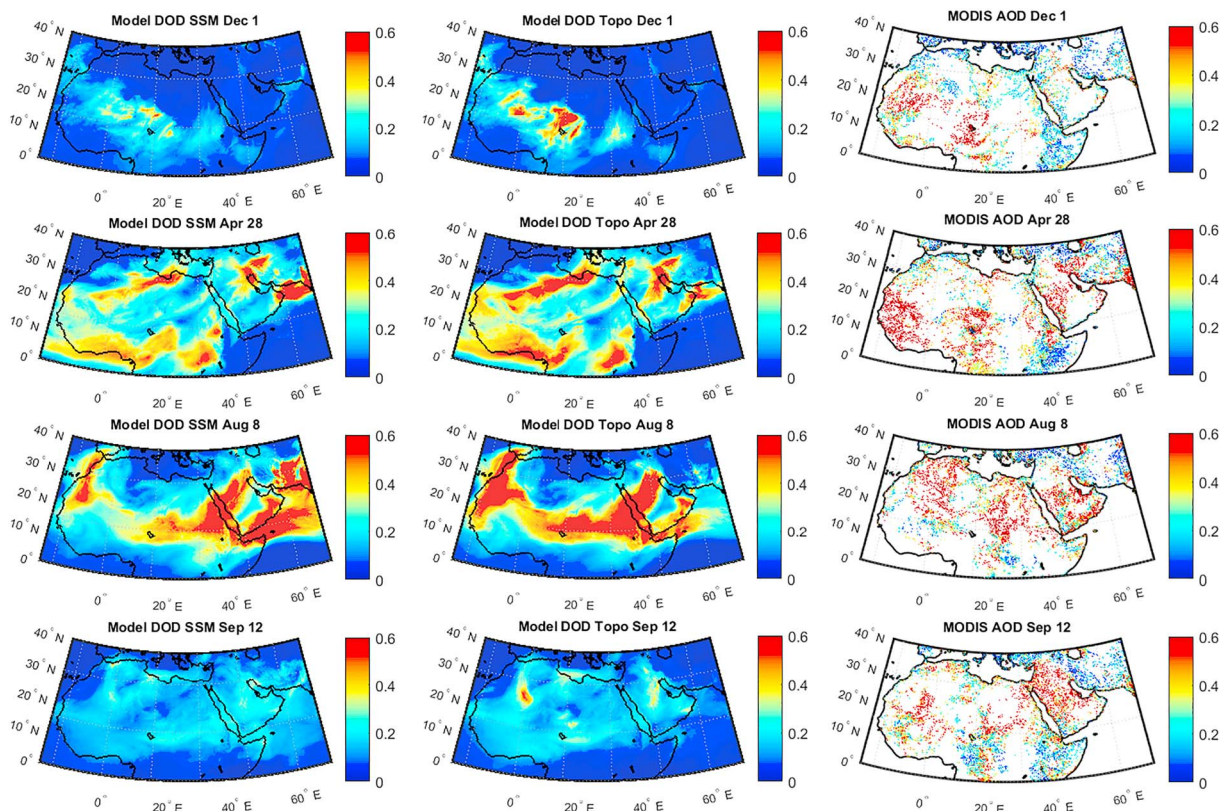

Figure 5. Model simulated dust optical depths (DODs) as compared to Moderate Resolution Imaging Spectroradiometer (MODIS) aerosol optical depth for four dusty days of 2015. The 4 days represent the days in which daily-mean aerosol optical depth was highest at KAUST in each season.
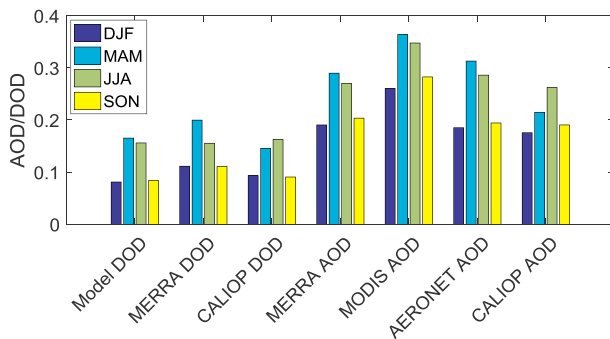
Figure 6. Comparison of model-simulated dust optical depth (DOD) with Modern-Era Retrospective Analysis for Research and Applications (MERRA), Moderate Resolution Imaging Spectroradiometer (MODIS), Aerosol Robotic Network (AERONET), and Cloud-Aerosol Lidar with Orthogonal Polarization (CALIOP) aerosol optical depth (AOD)/DOD for 2015. For all gridded data, reported AOD/DOD is the seasonal mean values at the grids containing all AERONET stations.
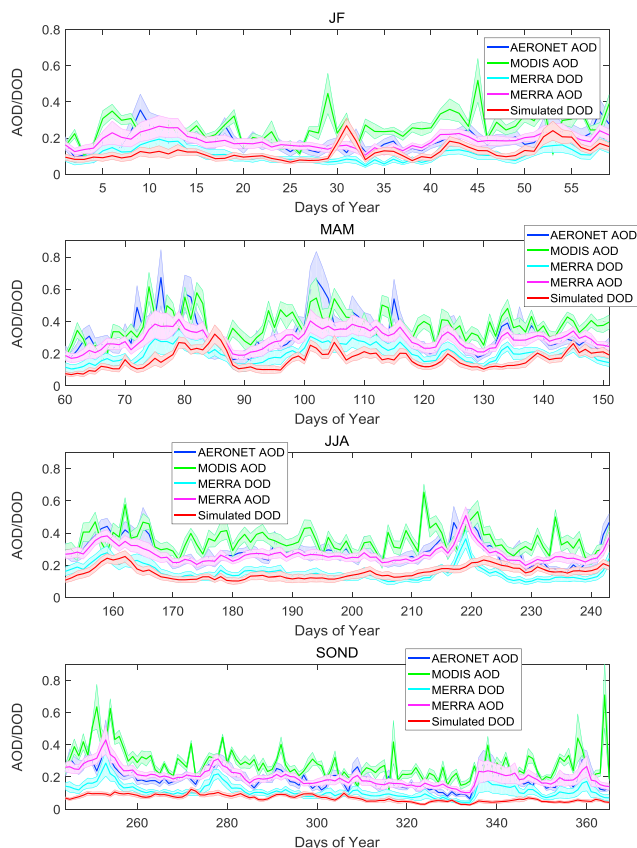
AODs are also consistent among all datasets, with only a small discrepancy caused by the inherent differences in the type of data, resolution, and sampling frequencies. The difference between AOD and DOD characterizes the contribution of aerosols, other than dust. In spring and summer, the total AOD is mostly consisted of dust. However, in fall and winter, almost 50% of the AOD are caused by other aerosols such as biomass burning, anthropogenic pollution, or sea-salt, depending upon the location.

Figure 7 shows the temporal variability of simulated daily average DOD, compared with AERONET, MODIS, and MERRA data, for all seasons. The simulated DOD compares well with the MERRA DOD. Differences between simulated DOD and assimilated MERRA-2 DOD is mainly due to the differences in the source function and the spatial resolution between our model and the MERRA-2 dust model. MODIS and AERONET values exhibit a higher temporal variability compared with the model/MERRA DOD values in all seasons.

Figure 8 shows the skill scores between the model-simulated DOD and MODIS AOD calculated for all the grid cells of MODIS data for each season. The skill scores are generally high, well above 0.5, in most dust source locations. The skill scores are generally higher in winter, spring, and summer and lower in fall. Overall, the model performs well in the study region including North Africa and the Arabian Peninsula. Skill scores are high in the Tigris-Euphrates region, and this is especially pronounced in winter and spring. In summer, MODIS AOD data are not available in many grid cells of the Tigris-Euphrates region, which explains why the map shows more empty cells in that region. The skill scores are high in the western Arabian Peninsula in summer. The model also shows good skill scores in the dust source regions between the Iran/Afghanistan/Pakistan basins, for all seasons. High scores are also observed in East Africa, including Sudan and Ethiopia, especially in spring and summer. Dust frequently gets transported from these areas to the Arabian Peninsula, especially in summer. Overall, the skill scores are satisfactory despite the fact that MODIS instrument scans a particular location only twice a day (10:30 a. m. and 01:30 p.m. local time). We also calculate the skill scores for AERONET AOD using all available stations, which are presented in Figure 9. Skill scores are high in most stations over spring and summer, and degrade during fall. Scores vary greatly by seasons. These skill scores are largely consistent with those calculated using MODIS data.

3.2.2. Dust Concentration and Particle Size Distribution

Figure 10 shows the sensitivity of the column-integrated volume PSD to the fraction of clay in surface emissions. Shown in the figure are the simulated dust and AERONET-retrieved aerosol in terms of vertically integrated volume PSD, for 2 clay-fraction scenarios at two representative stations.

Variation in the clay fraction seems to have a different impact in different stations. For example, at KAUST, which lies in the Arabian Peninsula, the medium clay-fraction scenario (20%) shows better agreement with AERONET data compared to the low clay-fraction scenario (4%), as shown in Figure 10. The amount of coarse dust is overestimated in the 4% clay scenario, but it is in good agreement with AERONET data in the 20% clay scenario. In contrast, at Dakar in West Africa, the 4% scenario compares better with AERONET PSD than the 20% scenario. Because our focus is on the Arabian Peninsula, we use the medium clay
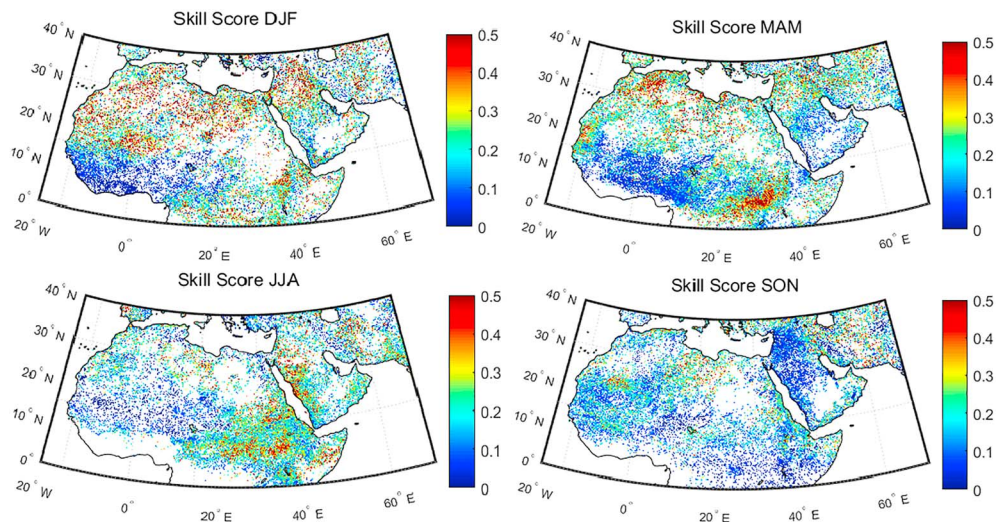

Figure 7. Temporal patterns of model-simulated dust optical depth (DOD), compared with Aerosol Robotic Network (AERONET), Moderate Resolution Imaging Spectroradiometer (MODIS), and Modern-Era Retrospective Analysis for Research and Applications (MERRA) aerosol optical depth (AOD)/DOD data, for all seasons of 2015, using daily means. Shades represent the standard error over all AERONET stations, for AERONET AOD, and the standard error of corresponding grid cells containing AERONET stations, for our model, MODIS, and MERRA AOD/DOD.

Figure 8. Skill scores calculated between model-simulated dust optical depth and Moderate Resolution Imaging Spectroradiometer (MODIS) aerosol optical depth, for four seasons, December–February (DJF), March–May (MAM), June–August (JJA), and September–November (SON). The white areas indicate that the MODIS aerosol optical depth data are not available in these grid cells.

fraction (20%) scenario in all of our simulations. The results of the comparison of all three scenarios mentioned in section 2.4 for all 15 stations are presented in the supporting information (Figure S5). The medium clay fraction scenario shows the best agreement with the PSDs in most AERONET stations. Generally, the low clay fraction (high clay fraction) scenario overestimates (underestimates) the coarse-mode fraction when compared to AERONET data.

We wish to emphasize that the size distribution of emitted dust in WRF-Chem is fixed and does not vary spatially, either for lack of observations or for computational efficiency. Wind tunnel experiments show that the emitted PSD depends on the parent soil properties (Parajuli, Zobeck, et al., 2016; Shao, 2001). Therefore, it is reasonable to expect that the emission fractions may depend on the parent soil properties. This issue may be addressed, to some extent, by deriving a spatial map of emission fractions from available soil data such as clay fraction. However, this is beyond the scope of the present study.

Figure 11 shows the simulated volume concentration, by particle size, in comparison with AERONET data from 15 stations over the summer period. Note that these results correspond to the 20% clay fraction scenarios mentioned earlier in section 2.4. In general, results from the model are in good agreement with AERONET data, for most stations, with respect to the magnitude of concentrations. For example, simulated dust concentrations are generally high at the KAUST station but low at the Tabernas station, in agreement with the AERONET data. A few stations in West Africa, including Banizoumbou and Dakar, exhibit much higher concentrations than the simulations. This is understandable because the West African region is greatly affected by biomass-burning aerosols (Bond et al., 2013). Since we only include dust aerosols in our simulations, the simulated concentrations appear lower.

The size range of the model is similar to that of AERONET. Although the model only simulates dust particles with radius less than 10 μm, almost all the aerosols appear to fall within this size range in the AERONET PSD. AERONET PSD shows a bimodal distribution in most of the stations with two peaks centered on ~0.1 μm and ~2–3 μm. We believe that the smaller second peak corresponds to the presence of either pollution or biomass burning aerosols depending upon the region, both of which are regarded as fine-mode aerosols. Such a bimodal distribution cannot be seen in the model results, since it has a limited number of bins (five only), which is not enough to resolve such level of detail contained in the AERONET data. Overall, our model is in good agreement with AERONET data, in terms of both concentration and size range. Results for the other seasons are quite similar and presented in Figure S6.

Figure 12 shows the simulated surface dust concentrations at the lowest model level as compared to MERRA reanalysis data. In general, MERRA surface dust concentrations are higher than the model concentrations,
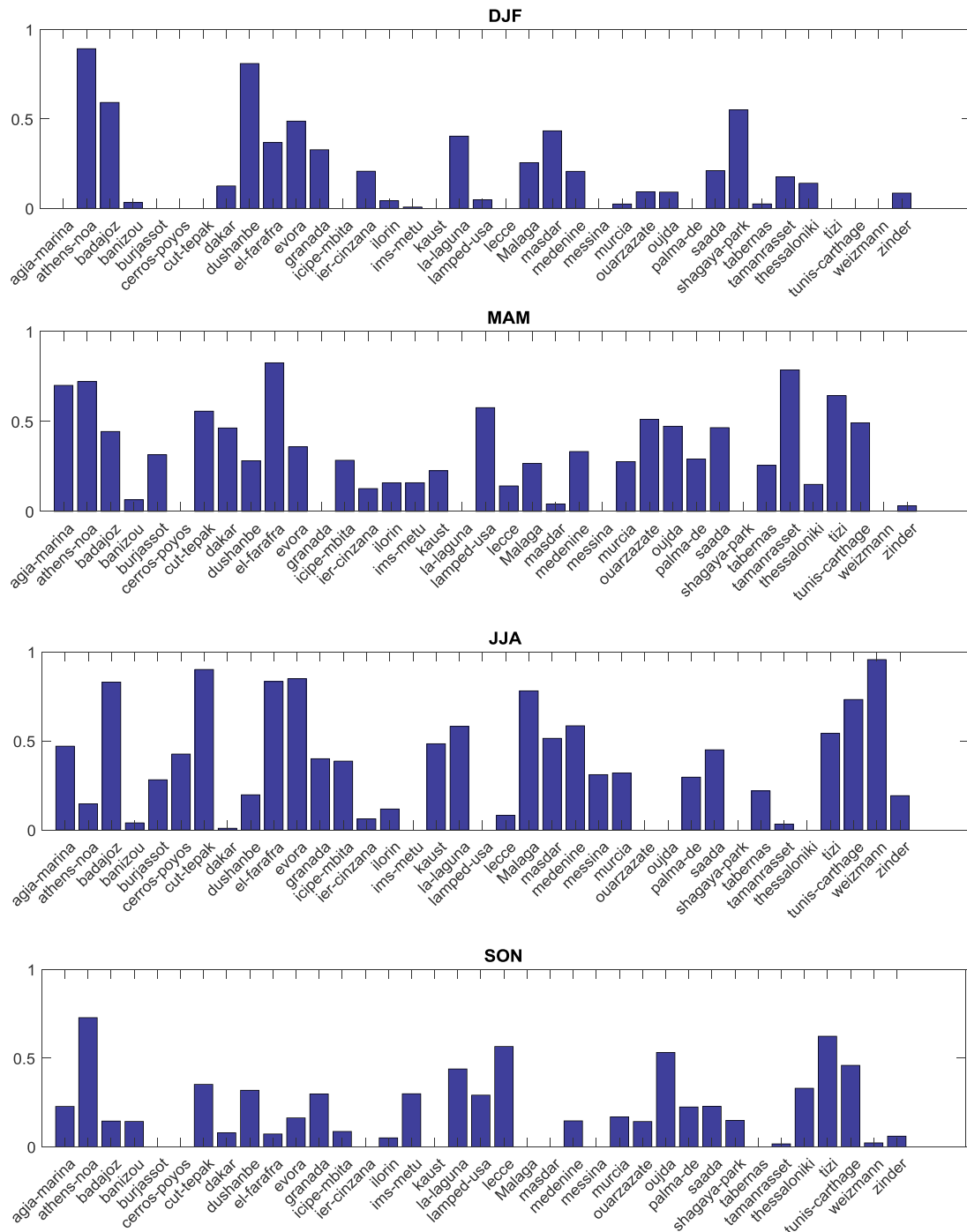
Figure 9. Skill scores between simulated dust optical depth and Aerosol Robotic Network (AERONET) aerosol optical depth, for different stations, and for (a) December–February (DJF), (b) March–May (MAM), (c) June–August (JJA), and (d) September–November (SON).

which is consistent with the higher values of dust optical depth in MERRA compared to the model simulations (Figure 6). In Tehran, Aleppo, and Muscat, the simulated surface dust concentrations agree well with those of MERRA. The difference in MERRA and model concentrations arises due to several reasons including the difference in tuning constraint applied, the difference in spatial resolution (4×4 km for Model and 0.5×0.625° for MERRA), and the difference in dust source function used (SSM in model and topographic in MERRA). Given these differences, the order of surface dust concentrations simulated by the
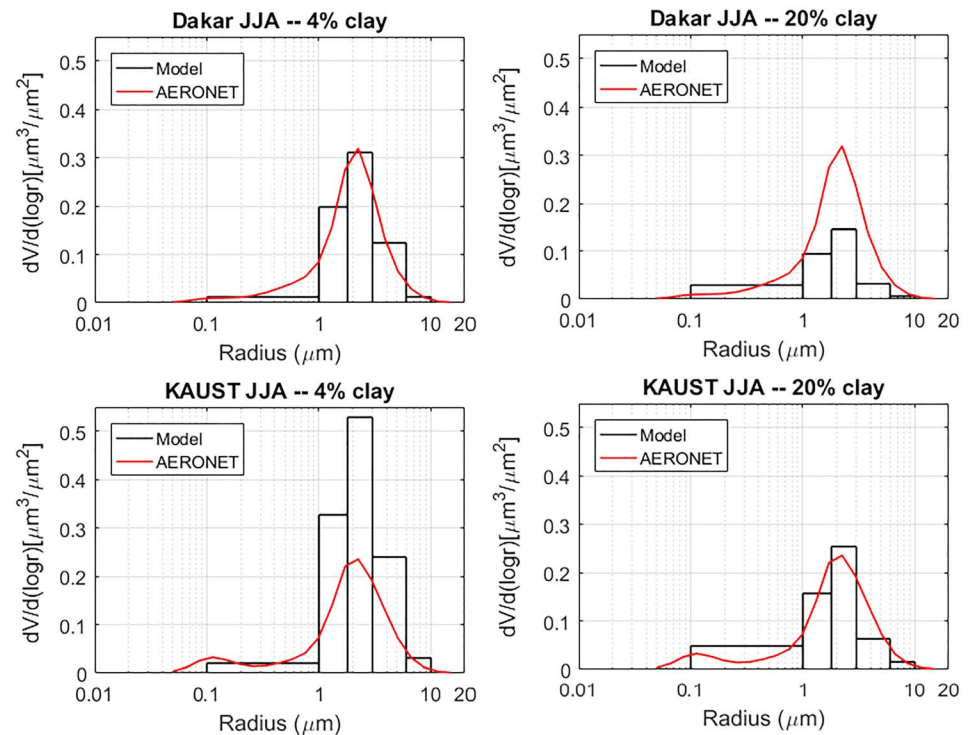
Figure 10. Summer-mean (2015) column-integrated volume concentrations from the model, in comparison with the Aerosol Robotic Network (AERONET) aerosol volume-distribution-function, for two size fractions scenarios, at two representative stations at KAUST (Saudi Arabia) and in Dakar (Senegal).

model are reasonable. Since dust is the main constituent of PM10 or PM2.5 in the region, these results further suggest that our simulated PM10 or PM2.5 are realistic.

3.3. Dust Emission and Transport From the Tigris-Euphrates Basin

In this section, we discuss the effect of Tigris-Euphrates dust sources on the air quality of the downwind regions. All the results presented here are derived from the nested simulations with the 4-km inner domain (shown below) covering the Arabian Peninsula.

As shown in Figure 13, the dust emitted from the Tigris-Euphrates region is responsible for high PM10 concentrations in the source areas that spread mostly to the south/southeast. Dust is also transported toward the northeast including Afghanistan and Pakistan over spring and fall. However, this phenomenon is more intensive in summer. Surface dust concentrations decrease as the dust plumes move downwind, and surface PM10 concentrations are lowest in winter, with less transport of dust in the downwind region during this season. The spatial pattern for PM2.5 concentration is very similar to that of PM10 (see details in Figure S7).

Figure 14 shows the spatial patterns of prevailing winds and dust emissions over the Tigris-Euphrates source region in summer (JJA) when dust transport over the Arabian Peninsula is highest. Figure 14a shows the exact locations of the dust sources from where the dust is transported across the entire Arabian Peninsula. The use of the SSM source function enables the model to produce a fine structure of dust emission; this would not be possible using the existing coarse-scale source functions. The emission is generally high in the northwest (~35°N, 40°E) where the sand deposits are abundant, and southeast (~33°N, 46°E), where the dominant land cover types are playas (Parajuli et al., 2014). Both sand deposits and playas are favorable surfaces for dust emission (Crouvi et al., 2012; Parajuli & Zender, 2017; Prospero et al., 2002). These hotspots for dust emission overlap with the surface wind maxima (Figure 14b). High winds in the northwest get channeled in the valley that stretches from the northwest to southeast, which is a typical characteristic of the Shamal winds.
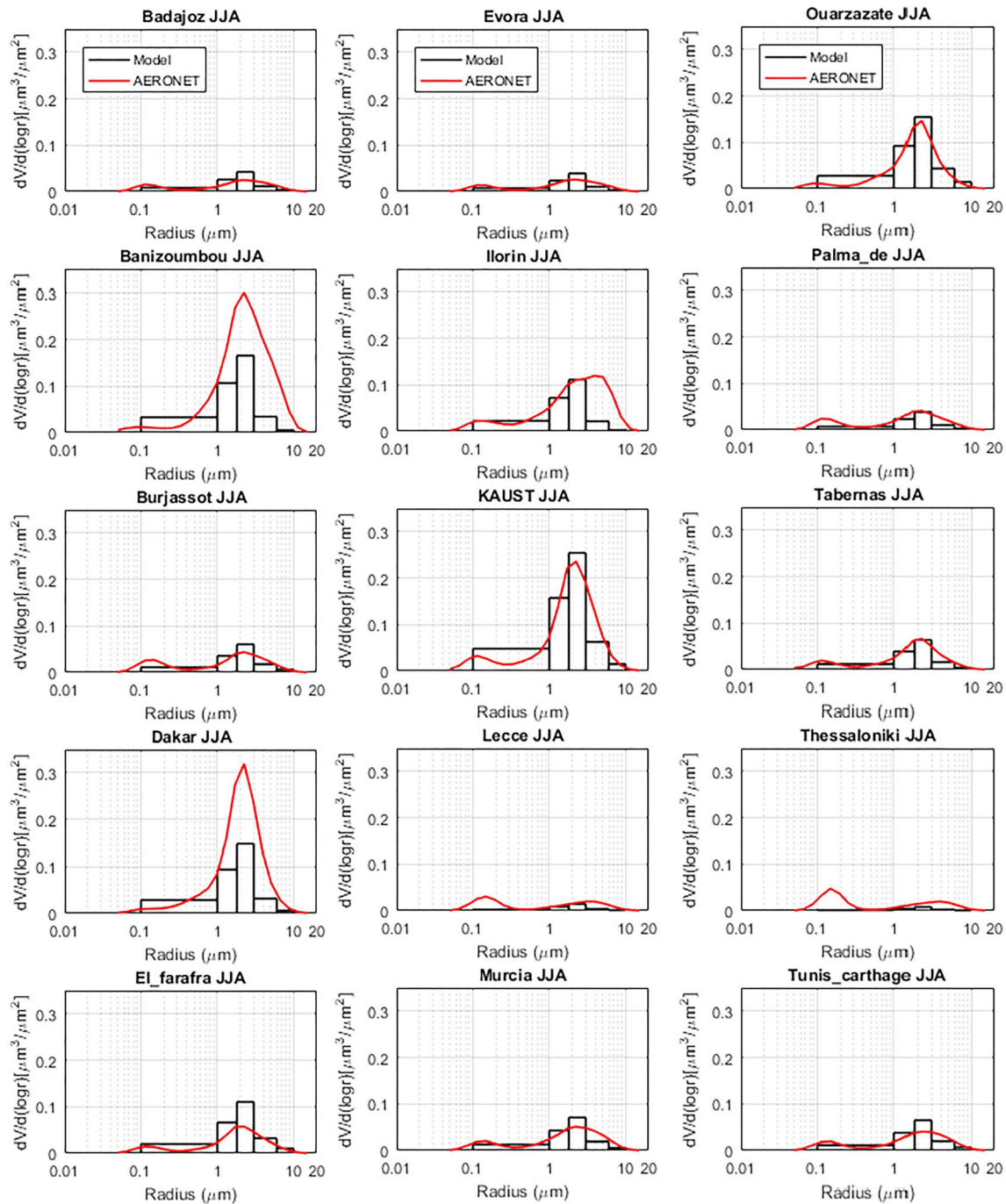
Figure 11. Mean column-integrated dust volume concentrations for summer (2015), in comparison with the Aerosol Robotic Network (AERONET) aerosol volume-distribution-function, at 15 stations.

Figure 15 shows the temporal profiles of simulated PM10 and PM2.5 daily mean surface concentrations, at nine of the most populated cities of the Middle East. The red horizontal lines in Figures 15a and 15b mark the U.S. Environmental Protection Agency standards for PM10 and PM2.5, respectively. All cities exceed U. S. standards for PM10, at least once per year, except for Jeddah and Sanaa. Similarly, all those cities exceeding the PM10 standard also exceed the PM2.5 standard, at least once a year. Note that, Muscat, which lies farthest downwind from the source region, exceeds the standard for both PM10 and PM2.5. In general, PM2.5 standards are exceeded more frequently than the PM10 standards for any of the cities. For
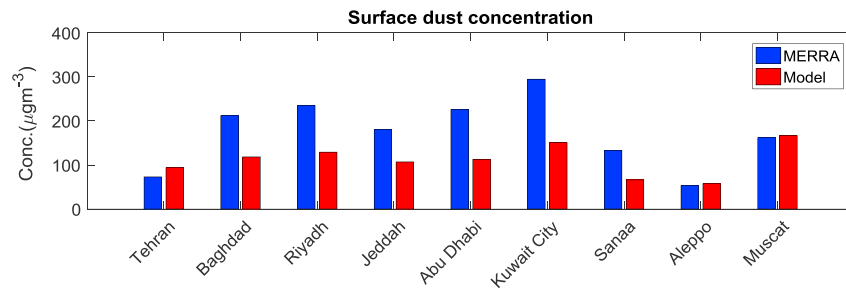
Figure 12. Comparison of surface dust concentrations (average for 2015) in Modern-Era Retrospective Analysis for Research and Applications (MERRA) data and model simulations at nine cities of the Middle East.

example, in Abu Dhabi, standards for PM10 and PM2.5 are exceeded for 12 and 21 days, respectively, over the course of the year. Similarly, in Muscat, the PM10 standard is exceeded only once a year, whereas the PM2.5 standard is exceeded three times a year. This is consistent with the fact that finer particles, which are of greater concern to health, can travel distances of several thousand kilometers before they are deposited. Our results clearly show that dust originating from the Tigris-Euphrates sources alone can severely affect the air quality in the downwind cities, even at great distances.
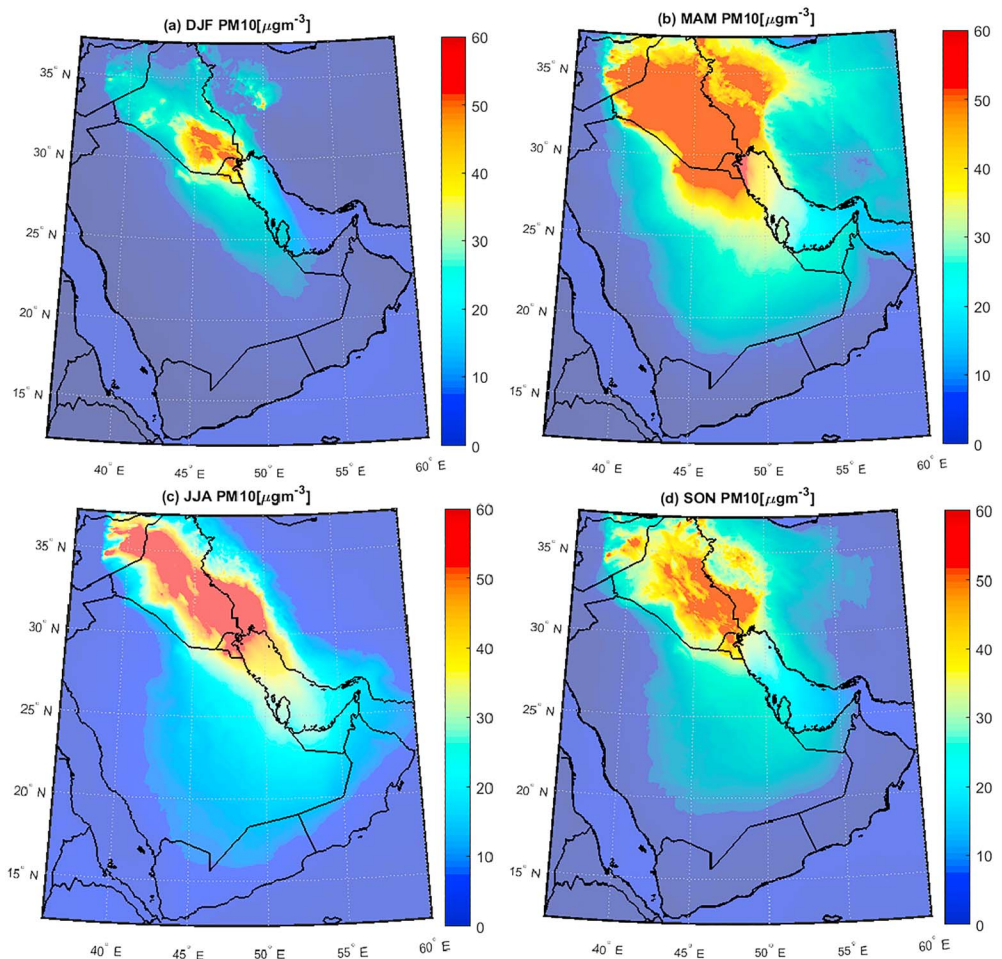

Figure 13. Model-simulated particulate matter (PM) 10 concentrations, at the lowest model level, by season for the year of 2015, and for Tigris-Euphrates dust sources only.
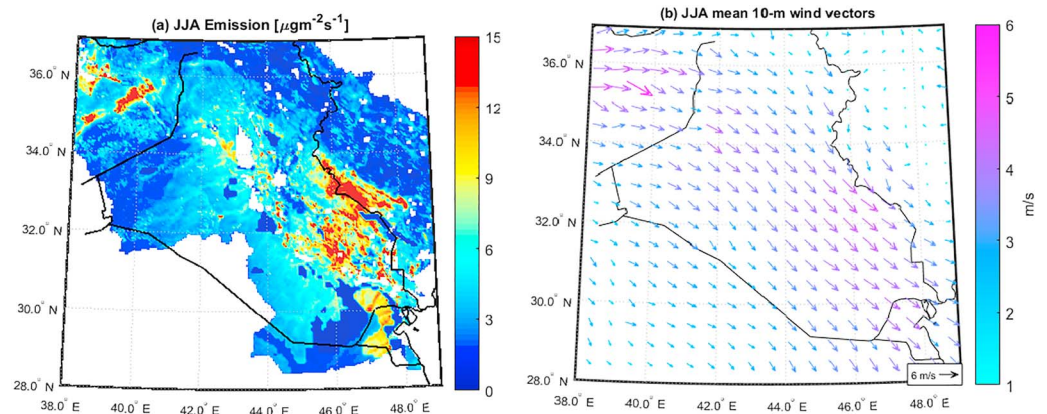
Figure 14. (a) Mean 10-m wind vectors; (b) average dust emission fluxes, in Summer (2015), and over the Tigris-Euphrates basin.

Figure 16 shows the contribution of the dust sources of the Tigris Euphrates river basin to the total dust concentration, over the region, during the dustiest season (JJA). Figure 16a shows the contribution (in percentage) of the surface PM10 concentrations (lowest level), and Figure 16b shows the contribution of the total columnar DOD. This contribution decreases southward, due to the gradual deposition of coarser dust particles during transport.

Contribution patterns for PM10 and DOD show different characteristics. For PM10, the contribution is greater in the Tigris-Euphrates source regions than in more distant locations. This is because surface dust dominates in these source regions, causing a higher contribution to PM10 than to DOD. This can be illustrated by examining the spatial extent of the contour lines. For example, the 50% contour (red line) near the source region is much wider for PM10 than for DOD. In the distant locations, the opposite is true; contours for DOD are wider than for PM10. As the distance from the source increases, the contribution of distant sources is higher for DOD than it is for PM10 due to the fact that DOD contains a stronger signal of long-range fine dust transport in the higher atmosphere. For this reason, the 10% contour (dark blue) for DOD is wider than for PM10.

Figure 15. (a) Particulate matter (PM) 10- and (b) PM2.5-simulated surface dust concentrations, with the Tigris Euphrates basin as dust source, for nine of the most populated cities of the Middle East.

In areas where the contribution is lower, there is more dust from sources other than Tigris-Euphrates sources. For example, in the western and southern Arabian Peninsula, there is little effect of the Tigris-Euphrates source, meaning that the air quality in these regions is more affected by North African and local dust sources.

The contribution patterns of PM10 and DOD for all seasons are presented in Figures S8 and S9. The contribution patterns in terms of PM2.5 are found to be quite similar to those of PM10. They are also presented in Figure S10.

Figure 17 shows the seasonal dust source contributions of the Tigris-Euphrates dust sources to the total amount of dust in the nine biggest cities. Contributions are generally higher in summer and fall than in winter and spring. It is evident that this contribution is remarkable, even in cities that are located far away from the Tigris-Euphrates region. For example, in Riyadh, summer contributions in terms of PM10 and DOD are about 35% and 39%, respectively. Similarly, in Abu Dhabi, which is very far from the Tigris-Euphrates source region, the summer contribution is about 42% in terms of PM10, and 28% in terms of DOD. In Muscat, which is farthest downwind, the contribution is about 15% for both PM10 and DOD in summer. These results clearly highlight the importance of the Tigris-Euphrates dust sources with respect to the air quality in the downwind region.
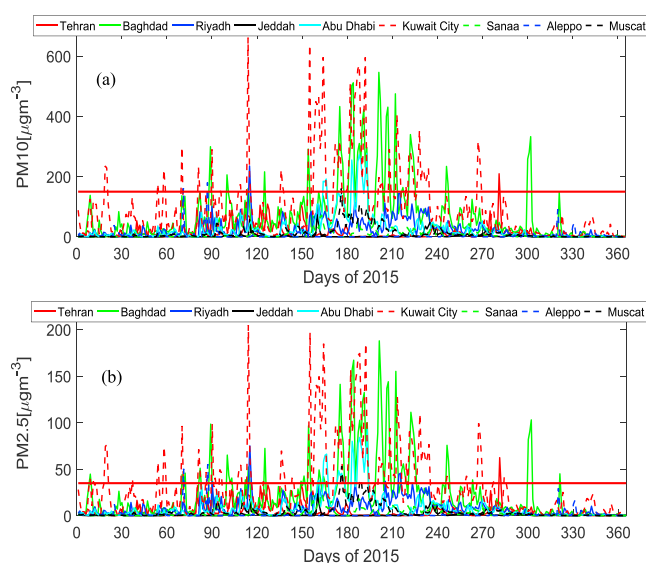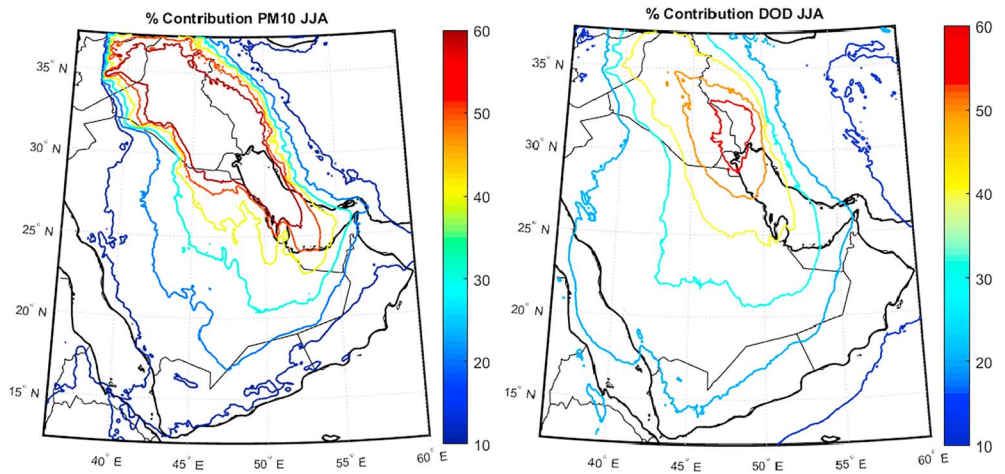
Figure 16. Contribution (in percentage) of the Tigris-Euphrates river basin to the total amount of dust in summer, in terms of (a) surface particulate matter (PM) 10 concentrations (b) total columnar dust optical depth (DOD). The colored contour lines range from 10 to 60% with an increment of 10, as shown in the color bar.
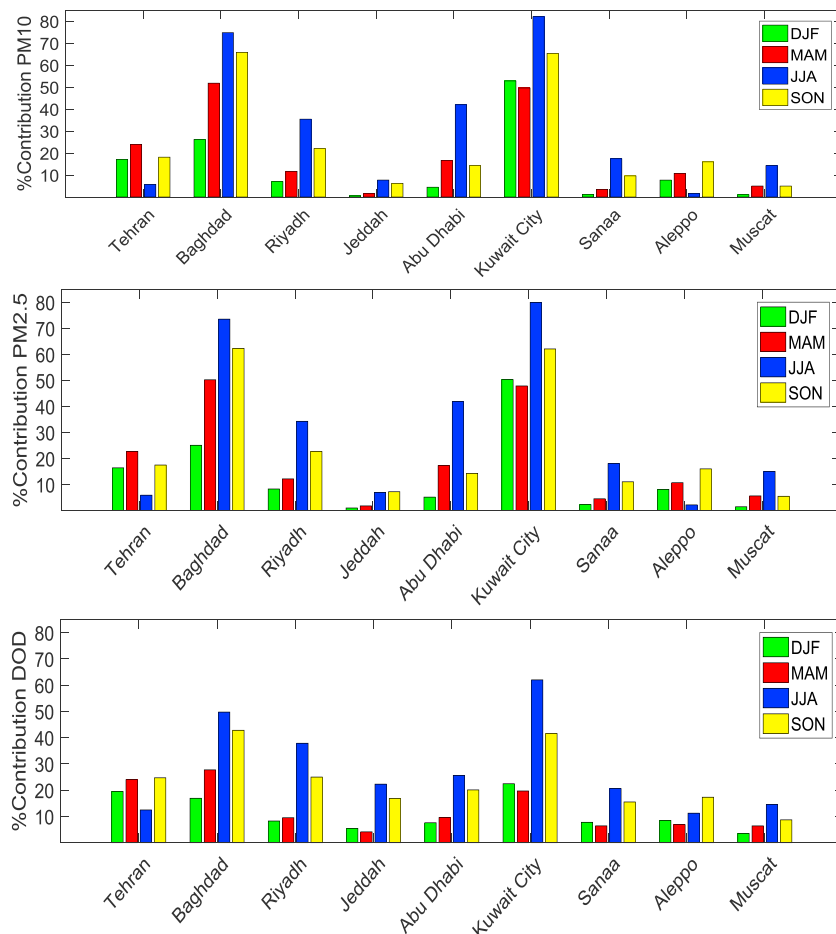

Figure 17. Contribution (%) of the Tigris-Euphrates dust sources to the total dust in different cities of the Arabian Peninsula for particulate matter (PM) 10, PM2.5, and dust optical depth (DOD).

4. Discussion and Conclusion

In this study, we conducted simulations of dust emission and transport over the MENA using a regional model and investigated three important research questions. First, we examined how a high-resolution dust source function performs in WRF-Chem. We found that a new, sediment-supply-based source function can be reliably used for high-resolution dust modeling over the MENA region to identify point-scale dust sources. Secondly, we tuned dust emission in WRF-Chem and achieved results that are consistent with observations in terms of all key parameters including dust optical depth, dust concentrations, and size distributions. We compared the results comprehensively with a set of observational and reanalysis data at a regional scale, focusing on the MENA region. Our results were generally in agreement with all datasets, including MODIS, CALIOP, AERONET, and MERRA. Finally, using the new source function at 4-km resolution, we also investigated how the dust emitted from the Tigris-Euphrates basin affect the air quality of the downwind region and determined the contribution of Tigris-Euphrates dust sources on the total dust concentration over the Arabian Peninsula. We show that the dust emitted from the Tigris-Euphrates region can affect the air quality of the entire Arabian Peninsula. Simulated surface dust concentrations resulting from the dust emitted from the Tigris-Euphrates basin exceeded the 24-hr-average standard of 150 $\mu g/m^3$ for PM10 in seven of the nine downwind cities considered, namely, Tehran, Baghdad, Riyadh, Abu Dhabi, Kuwait City, Aleppo, and Muscat; the only exceptions were Jeddah and Sanaa. Similarly, the PM2.5 standard of 35 $\mu g/m^3$ was also exceeded in those seven cities.

4.1. Implications of High-Resolution Source Function

Dust emission and transport simulated by commonly used climate models are often far from reliable (Evan et al., 2014); one reason for this discrepancy is the poor representation of "dust sources" in the models. The dust modeling community has realized the need to better characterize dust sources in models in order to improve the estimation of dust emission fluxes. Several recent studies have contributed to the development of model-friendly, high-resolution dust source functions (e.g., Ginoux et al., 2012; Kim et al., 2012; Koven & Fung, 2008; Lary et al., 2016; Parajuli & Zender, 2017; Walker et al., 2009). In this context, we conduct dust simulations at a high resolution using a newly developed dust source function in WRF-Chem over the MENA region.

Evidently, the problem of correctly representing dust sources in regional/global dust models cannot be addressed solely by using a high-resolution source function. For example, our new source function identifies several new small-scale dust sources; consequently, the simulated dust emission is higher and shows localized maxima of dust in some locations (Figure 14b). In addition, when using any high-resolution dataset, some structural changes are required in order to optimize the performance of the new source function in the model. Clearly, this is a matter of concern for the entire dust modeling community. Further efforts are therefore needed to develop an improved framework that better uses high-resolution data. The first step may be to "inform" the source function with a dust source geomorphology using land cover types (Baddock et al., 2016; Parajuli & Zender, 2017).

We evaluated the new source function over the MENA region where more than 50% of global dust sources are located. However, additional studies are needed for testing this source function's performance in other regions of the world. Because of its high-resolution, the use of a new source function would be more beneficial in small-scale studies focusing on finer-scale heterogeneity of the dust sources. This would enable the identification of the exact source areas in order to determine how the emitted dust relates to geomorphology (e.g., Baddock et al., 2016; Feuerstein & Schepanski, 2019; Parajuli & Zender, 2017). Such studies can benefit from the high-resolution, high-frequency satellite data such as SEVIRI (e.g., Brindley et al., 2015; Schepanski et al., 2007), which enables the tracking of individual dust events.

It is important to highlight the underlying discrepancies in the observational datasets used in this study. First, AERONET data exclude nighttime dust events, and MODIS data capture dust events only twice a day (10.30 a.m. and 1:30 p.m. local time); therefore, both sources may cause some bias in the data. Second, satellite AOD values are underestimated in convective regions because of the undersampling of AOD caused by cloud cover. On the other hand, they are overestimated over morning source regions such as the Bodélé Depression because of their diurnal variability (Kocha et al., 2013). Unfortunately, many of the dust events, such as haboob (e.g., Khan et al., 2015), are followed by severe weather conditions for

which the presence of clouds restricts the retrieval of AOD by MODIS and AERONET instruments, thus missing such important dust events. Third, although we use a large number of AERONET stations, they are primarily located in coastal regions, despite the fact that most of the dustiest areas lie inland. All these problems are minor; nevertheless, they do highlight the need for more observational data in dust-related research (Evan et al., 2014).

It is generally known that most dust activities are caused by Shamal winds (Francis et al., 2017; Rao et al., 2003) over the Middle East (in both summer and winter) and Harmattan winds (Koren et al., 2006; McTainsh, 1980) over North Africa (winter and spring). Although some seasons are more favorable for dust emissions, dust events can occur at any period of the year, for a given location, as shown by the high dust concentration values reached in all seasons (Figure 13). We also find that there is a high spatial variability in dust emissions across the study region (Figure 4). In the Sahel area, where vegetation cover is lowest and winds frequently exceed the threshold friction velocity, more than 70% of dust events occur from mid-April to mid-July (Bergametti et al., 2017). Dust emission also has a strong diurnal variability. For example, over the Sahara, most dust events occur in the morning (0600–0900 UTC) and are caused by the breakdown of the nocturnal low-level jet (Schepanski et al., 2009). Similarly, contributions from other aerosol types may differ depending on the region, which adds complications in studying the origin and transport of dust aerosols, using satellite data. For example, the highest biomass-burning season is DJF in North Africa (Horowitz et al., 2017). These are only some examples that highlight the challenges of modeling dust emission and transport over the MENA region.

4.2. Impact of Tigris-Euphrates Dust Sources

The Tigris-Euphrates basin is a key dust source region for the MENA. In this study, we examined how the dust originating from Tigris-Euphrates area affects the regional air quality. The significant transport of dust from the Tigris-Euphrates region to the downwind Arabian Peninsula in summer observed in this study is consistent with that from previous studies (e.g., Reid et al., 2008). The sources of dust in the Arabian Peninsula can be classified into four main groups: the Tigris Euphrates basin, the basins of Iran/Pakistan/ Afghanistan, Northeast Africa, and local sources (Reid et al., 2008). Sotoudeheian et al. (2016) found that the Tigris-Euphrates region contributes about 95% and 76% of the dust aerosols in the two Iranian cities Ahvaz and Tehran, respectively. Our findings are largely consistent with these results but provide more spatio-temporal details of the contribution of dust from the Tigris-Euphrates basin, to the entire Arabian Peninsula. Our findings support the observations that regional large-scale phenomena dominate the temporal variability of dust over local effects in the Arabian Peninsula (Eck et al., 2008).

Dust emission from the Tigris-Euphrates basin has further implications because of the DU used in the Iraq-Kuwait region during the 1991 Gulf War, which has become a matter of public concern. DU can be used as a "tracer" for the transport and deposition of pollutants in the region. The air and soil samples collected in several countries of the Middle East have shown evidence of DU contamination (Bešić et al., 2018). The DU contamination in the downwind region supports our finding that dust originating from the Tigris-Euphrates river basin spreads to an entire downwind region of the Arabian Peninsula.

The issue of DU contamination in the region is often discussed under the heading "Gulf War Syndrome" because of its possible impact on human health (Bem & Bou-Rabee, 2004; Bešić et al., 2018). Several past studies (e.g., Bem & Bou-Rabee, 2004; Bou-Rabee et al., 1995; Luckett, 2006) have analyzed soil and water samples from Kuwait and found that DU did not cause significant "radiological hazard" to human beings. However, it is well-established that uranium can enter the human body by various pathways, including "inhalation" (Ababneh et al., 2017; Bem & Bou-Rabee, 2004), which is of concern during dust storms.

According to the International Commission on Radiological Protection, the maximum safe level of uranium intake by inhalation in humans is 30 Bq per year (Bou-Rabee et al., 1995). We estimated the minimum atmospheric uranium concentration that would cause an exceedance of this 30 Bq limit by assuming a specific activity of natural uranium of 24.5 Bq/kg, a standard breathing rate of ~28 m^3 air per day, and a 75% retention of PM in the respiratory system, following Bou-Rabee's calculations (Bou-Rabee et al., 1995). Our results show that the annual standard would be exceeded if the air concentration of uranium exceeds 0.16 $\mu g/m^3$. Measurements show that the ratio of PM concentration to uranium concentration in the air is approximately 6.78×10^5 (Bou-Rabee et al., 1995). Given this ratio, the corresponding dust PM concentration that would be

required to exceed the limit of 30 Bq would be approximately 108,000 μg/m³. This value is extremely high and is unlikely to be exceeded, even during the worst dust storms, in which dust concentrations do not reach more than a few thousand micrograms per cubic meters (e.g., Prakash et al., 2015).

We note that regional dust emission patterns will likely change under future climate-change-scenarios. For example, the Tigris-Euphrates region has been a conflict zone with a number of wars for many decades now and has recently experienced drought (Chao et al., 2017) and reduced agricultural activities (Woertz, 2017). All of these factors can increase dust emission and downwind transport of dust and other environmental pollutants. In addition, dust deposition could also accumulate in the natural environment where the rate of dust deposition is very high (Figure S11). Therefore, the possible mobilization of DU in the future and its effect on regional air quality should not be ruled out. Furthermore, several countries in the region have already installed, or are in the process of installing, nuclear reactors for energy production (Ahmad & Ramana, 2014; Khan et al., 2017). The detonation of nuclear weapons could lead to a multitude of negative effects such as mass fatalities, and severe disruption to agriculture and food security through changes in growing seasons across the much broader regions (Toon et al., 2007). Thus, we conclude that the management of the Tigris-Euphrates basin is a shared responsibility of all countries in the region, and an integrated and coordinated effort is essential to maintain air quality standards for all stakeholders and countries of the Middle East and indeed further afield.

AOT retrievals induce an underestimation of 0.28 (~40%) over the convective regions and an overestimation of 0.1 (17%) over morning source areas like Bodélé.

References

Ababneh, Z. Q., Ababneh, A. M., Alsagabi, S., & Almasoud, F. I. (2017). A study of the radioactivity in the dust storm event of April 2015 in Arabian Peninsula. *Radiation Protection Dosimetry*, *179*(2), 108–118. https://doi.org/10.1093/rpd/ncx221

Ahmad, A., & Ramana, M. V. (2014). Too costly to matter: Economics of nuclear power for Saudi Arabia. *Energy*, *69*, 682–694. https://doi.org/10.1016/j.energy.2014.03.064

Anisimov, A., Axisa, D., Kucera, P. A., Mostamandi, S., & Stenchikov, G. (2018). Observations and cloud-resolving modeling of Haboob dust storms over the Arabian Peninsula. *Journal of Geophysical Research: Atmospheres*, *123*, 12,147–12,179. https://doi.org/10.1029/2018JD028486

Anisimov, A., Tao, W., Stenchikov, G., Kalenderski, S., Prakash, P. J., Yang, Z.-L., & Shi, M. (2017). Quantifying local-scale dust emission from the Arabian Red Sea coastal plain. *Atmospheric Chemistry and Physics*, *17*, 1–43. https://doi.org/10.5194/acp-2016-723

Baddock, M. C., Ginoux, P., Bullard, J. E., & Gill, T. E. (2016). Do MODIS-defined dust sources have a geomorphological signature? *Geophysical Research Letters*, *43*, 2606–2613. https://doi.org/10.1002/2015GL067327

Basart, S., Vendrell, L., & Baldasano, J. M. (2016). High-resolution dust modelling over complex terrains in West Asia. *Aeolian Research*, *23*, 37–50. https://doi.org/10.1016/j.aeolia.2016.09.005

Bem, H., & Bou-Rabee, F. (2004). Environmental and health consequences of depleted uranium use in the 1991 Gulf War. *Environment International*, *30*(1), 123–134. https://doi.org/10.1016/S0160-4120(03)00151-X

Bergametti, G., Marticorena, B., Rajot, J. L., Chatenet, B., Féron, A., Gaimoz, C., et al. (2017). Dust uplift potential in the central Sahel: An analysis based on 10 years of meteorological measurements at high temporal resolution. *Journal of Geophysical Research: Atmospheres*, *122*, 12,433–12,448. https://doi.org/10.1002/2017JD027471

Bešić, L., Muhović, I., Mrkulić, F., Spahić, L., Omanović, A., & Kurtovic-Kozaric, A. (2018). Meta-analysis of depleted uranium levels in the Middle East region. *Journal of Environmental Radioactivity*, *192*, 67–74. https://doi.org/10.1016/j.jenvrad.2018.06.004

Bond, T. C., Doherty, S. J., Fahey, D. W., Forster, P. M., Berntsen, T., DeAngelo, B. J., et al. (2013). Bounding the role of black carbon in the climate system: A scientific assessment. *Journal of Geophysical Research: Atmospheres*, *118*, 5380–5552. https://doi.org/10.1002/jgrd.50171

Bou-Rabee, F., Bakir, Y., & Bem, H. (1995). Contribution of uranium to gross alpha radioactivity in some environmental samples in Kuwait. *Environment International*, *21*(3), 293–298. https://doi.org/10.1016/0160-4120(95)00022-D

Brindley, H., Osipov, S., Bantges, R., Smirnov, A., Banks, J., Levy, R., et al. (2015). An assessment of the quality of aerosol retrievals over the Red Sea and evaluation of the climatological cloud-free dust direct radiative effect in the region. *Journal of Geophysical Research: Atmospheres*, *120*, 10,862–10,878. https://doi.org/10.1002/2015JD023282

Chao, N., Luo, Z., Wang, Z., & Jin, T. (2017). Retrieving groundwater depletion and drought in the Tigris-Euphrates Basin between 2003 and 2015. *Groundwater*, *56*(5), 770–782. https://doi.org/10.1111/gwat.12611

Chen, F., & Dudhia, J. (2001). Coupling an advanced land surface/hydrology model with the Penn State/NCAR MM5 modeling system. Part I: Model description and implementation. *Monthly Weather Review*, *129*(4), 569–585. https://doi.org/10.1175/1520-0493(2001)129<0569:CAALSH>2.0.CO;2

Cremades, P. G., Fernández, R. P., Allende, D. G., Mulena, G. C., & Puliafito, S. E. (2017). High resolution satellite derived erodibility factors for WRF/Chem windblown dust simulations in Argentina. *Atmósfera*, *30*(1), 11–25. https://doi.org/10.20937/ATM.2017.30.01.02

Crouvi, O., Schepanski, K., Amit, R., Gillespie, A. R., & Enzel, Y. (2012). Multiple dust sources in the Sahara Desert: The importance of sand dunes. *Geophysical Research Letters*, *39*, L13401. https://doi.org/10.1029/2012GL052145

Dubovik, O., & King, M. D. (2000). A flexible inversion algorithm for retrieval of aerosol optical properties from Sun and sky radiance measurements. *Journal of Geophysical Research*, *105*(D16), 20,673–20,696. https://doi.org/10.1029/2000JD900282

Eck, T. F., Holben, B. N., Reid, J. S., Dubovik, O., Smirnov, A., O'Neill, N. T., et al. (1999). Wavelength dependence of the optical depth of biomass burning, urban and desert dust aerosols. *Journal of Geophysical Research*, *104*(D24), 31,333–31,349. https://doi.org/10.1029/1999JD900923

Eck, T. F., Holben, B. N., Reid, J. S., Sinyuk, A., Dubovik, O., Smirnov, A., et al. (2008). Spatial and temporal variability of column-integrated aerosol optical properties in the southern Arabian Gulf and United Arab Emirates in summer. *Journal of Geophysical Research*, *113*, D01204. https://doi.org/10.1029/2007JD008944

Evan, A. T., Flamant, C., Fiedler, S., & Doherty, O. (2014). An analysis of aeolian dust in climate models. *Geophysical Research Letters*, *41*, 5996–6001. https://doi.org/10.1002/2014GL060545

Feuerstein, S., & Schepanski, K. (2019). Identification of dust sources in a Saharan dust hot-spot and their implementation in a dust-emission model. *Remote Sensing*, *11*(1). https://doi.org/10.3390/rs11010004

Flaounas, E., Kotroni, V., Lagouvardos, K., Klose, M., Flamant, C., & Giannaros, T. M. (2016). Assessing atmospheric dust modelling performance of WRF-Chem over the semi-arid and arid regions around the Mediterranean. *Atmospheric Chemistry and Physics Discussions*, 1–28. https://doi.org/10.5194/acp-2016-307

Francis, D. B. K., Flamant, C., Chaboureau, J.-P., Banks, J., Cuesta, J., Brindley, H., & Oolman, L. (2017). Dust emission and transport over Iraq associated with the summer Shamal winds. *Aeolian Research*, *24*, 15–31. https://doi.org/10.1016/j.aeolia.2016.11.001

Gelaro, R., McCarty, W., Suárez, M. J., Todling, R., Molod, A., Takacs, L., et al. (2017). The Modern-Era Retrospective Analysis for Research and Applications, Version 2 (MERRA-2). *Journal of Climate*, *30*(14), 5419–5454. https://doi.org/10.1175/JCLI-D-16-0758.1

Ginoux, P., Chin, M., Tegen, I., Prospero, J. M., Holben, B., Dubovik, O., & Lin, S. J. (2001). Sources and distributions of dust aerosols simulated with the GOCART model. *Journal of Geophysical Research*, *106*(D17), 20,255–20,273. https://doi.org/10.1029/2000JD000053

Ginoux, P., Prospero, J. M., Gill, T. E., Hsu, N. C., & Zhao, M. (2012). Global-scale attribution of anthropogenic and natural dust sources and their emission rates based on MODIS deep blue aerosol products. *Reviews of Geophysics*, *50*, RG3005. https://doi.org/10.1029/2012RG000388

Grell, G. A., & Freitas, S. R. (2014). A scale and aerosol aware stochastic convective parameterization for weather and air quality modeling. *Atmospheric Chemistry and Physics*, *14*(10), 5233–5250. https://doi.org/10.5194/acp-14-5233-2014

Grini, A., Myhre, G., Zender, C. S., & Isaksen, I. S. A. (2005). Model simulations of dust sources and transport in the global atmosphere: Effects of soil erodibility and wind speed variability. *Journal of Geophysical Research*, *110*, D02205. https://doi.org/10.1029/2004JD005037

Holben, B. N., Eck, T. F., Slutsker, I., Tanré, D., Buis, J. P., Setzer, A., et al. (1998). AERONET—A federated instrument network and data archive for aerosol characterization. *Remote Sensing of Environment*, *66*(1), 1–16. https://doi.org/10.1016/S0034-4257(98)00031-5

Horowitz, H. M., Garland, R. M., Thatcher, M., Landman, W. A., Dedekind, Z., van der Merwe, J., & Engelbrecht, F. A. (2017). Evaluation of climate model aerosol seasonal and spatial variability over Africa using AERONET. *Atmospheric Chemistry and Physics*, *17*(22), 13,999–14,023. https://doi.org/10.5194/acp-17-13999-2017

Hsu, N. C., Jeong, M. J., Bettenhausen, C., Sayer, A. M., Hansell, R., Seftor, C. S., et al. (2013). Enhanced Deep Blue aerosol retrieval algorithm: The second generation. *Journal of Geophysical Research: Atmospheres*, *118*, 9296–9315. https://doi.org/10.1002/jgrd.50712

Hsu, N. C., Tsay, S. C., King, M. D., & Herman, J. R. (2004). Aerosol properties over bright-reflecting source regions. *IEEE Transactions on Geoscience and Remote Sensing*, *42*(3), 557–569. https://doi.org/10.1109/TGRS.2004.824067

Iacono, M. J., Delamere, J. S., Mlawer, E. J., Shephard, M. W., Clough, S. A., & Collins, W. D. (2008). Radiative forcing by long-lived greenhouse gases: Calculations with the AER radiative transfer models. *Journal of Geophysical Research*, *113*, D13103. https://doi.org/10.1029/2008JD009944

Janjic, Z. (1994). The Step-Mountain Eta Coordinate Model: Further developments of the convection, viscous sublayer, and turbulence closure schemes. *Monthly Weather Review*, *122*(5), 927–945. https://doi.org/10.1175/1520-0493(1994)122<0927:TSMECM>2.0.CO;2

Jiménez, E., Linares, C., Martínez, D., & Díaz, J. (2010). Role of Saharan dust in the relationship between particulate matter and short-term daily mortality among the elderly in Madrid (Spain). *Science of the Total Environment*, *408*(23), 5729–5736. https://doi.org/10.1016/j.scitotenv.2010.08.049

Jones S. L., G. A. Creighton, E. L. Kuchera, E. A. Rentschler (2011). Adapting WRF-CHEM GOCART for Fine-Scale Dust Forecasting, AGU Fall Meeting Abstracts, 1.

Kalenderski, S., Stenchikov, G., & Zhao, C. (2013). Modeling a typical winter-time dust event over the Arabian Peninsula and the Red Sea. *Atmospheric Chemistry and Physics*, *13*(4), 1999–2014. https://doi.org/10.5194/acp-13-1999-2013

Khan, B., Stenchikov, G., Weinzierl, B., Kalenderski, S., & Osipov, S. (2015). Dust plume formation in the free troposphere and aerosol size distribution during the Saharan Mineral Dust Experiment in North Africa. *Tellus Series B: Chemical and Physical Meteorology*, *67*(1), 27,170. https://doi.org/10.3402/tellusb.v67.27170

Khan, S. U.-D., Khan, S. U.-D., Haider, S., El-Leathy, A., Rana, U. A., Danish, S. N., & Ullah, R. (2017). Development and techno-economic analysis of small modular nuclear reactor and desalination system across Middle East and North Africa region. *Desalination*, *406*, 51–59. https://doi.org/10.1016/j.desal.2016.05.008

Kim, D., Chin, M., Kemp, E. M., Tao, Z., Peters-Lidard, C. D., & Ginoux, P. (2012). Development of high-resolution dynamic dust source function—A case study with a strong dust storm in a regional model. *Atmospheric Environment*, *159*, 11–25. https://doi.org/10.1016/j.atmosenv.2017.03.045

Klingmüller, K., Metzger, S., Abdelkader, M., Karydis, V. A., Stenchikov, G. L., Pozzer, A., & Lelieveld, J. (2018). Revised mineral dust emissions in the atmospheric chemistry–climate model EMAC (MESSy 2.52 DU_Astitha1 KKDU2017 patch). *Geoscientific Model Development*, *11*, 989–1008. https://doi.org/10.5194/gmd-11-989-2018

Klose, M., Shao, Y., Li, X., Zhang, H., Ishizuka, M., Mikami, M., & Leys, J. F. (2014). Further development of a parameterization for convective turbulent dust emission and evaluation based on field observations. *Journal of Geophysical Research: Atmospheres*, *119*, 10,441–10,457. https://doi.org/10.1002/2014JD021688

Kocha, C., Tulet, P., Lafore, J.-P., & Flamant, C. (2013). The importance of the diurnal cycle of Aerosol Optical Depth in West Africa. *Geophysical Research Letters*, *40*, 785–790. https://doi.org/10.1002/grl.50143

Kok, J. F. (2011). A scaling theory for the size distribution of emitted dust aerosols suggests climate models underestimate the size of the global dust cycle. *PNAS*, *108*(3), 1016–1021. https://doi.org/10.1073/pnas.1014798108

Kok, J. F., Albani, S., Mahowald, N. M., & Ward, D. S. (2014). An improved dust emission model—Part 2: Evaluation in the Community Earth System Model, with implications for the use of dust source functions. *Atmospheric Chemistry and Physics*, *14*(23), 13,043–13,061. https://doi.org/10.5194/acp-14-13043-2014

Kontos, S., Liora, N., Giannaros, C., Kakosimos, K., Poupkou, A., & Melas, D. (2018). Modeling natural dust emissions in the central Middle East: Parameterizations and sensitivity. *Atmospheric Environment*, *190*, 294–307. https://doi.org/10.1016/j.atmosenv.2018.07.033

Koren, I., Kaufman, Y. J., Washington, R., Todd, M. C., Rudich, Y., Martins, J. V., & Rosenfeld, D. (2006). The Bodélé depression: a single spot in the Sahara that provides most of the mineral dust to the Amazon forest. *Environmental Research Letters*, *1*(1), 014005. https://doi.org/10.1088/1748-9326/1/1/014005

Koven, C. D., & Fung, I. (2008). Identifying global dust source areas using high-resolution land surface form. *Journal of Geophysical Research*, *113*, D22204. https://doi.org/10.1029/2008JD010195

Kumar, R., Barth, M. C., Pfister, G. G., Naja, M., & Brasseur, G. P. (2014). WRF-Chem simulations of a typical pre-monsoon dust storm in northern India: Influences on aerosol optical properties and radiation budget. *Atmospheric Chemistry and Physics*, *14*(5), 2431–2446. https://doi.org/10.5194/acp-14-2431-2014

Lary, D. J., Alavi, A. H., Gandomi, A. H., & Walker, A. L. (2016). Machine learning in geosciences and remote sensing. *Geoscience Frontiers*, *7*(1), 3–10. https://doi.org/10.1016/j.gsf.2015.07.003

LeGrand, S. L., Polashenski, C., Letcher, T. W., Creighton, G. A., Peckham, S. E., & Cetola, J. D. (2019). The AFWA dust emission scheme for the GOCART aerosol model in WRF-Chem v3.8.1. *Geoscientific Model Development*, *12*, 131–166. https://doi.org/10.5194/gmd-12-131-2019

Lehner, B., & Grill, G. (2013). Global river hydrography and network routing: Baseline data and new approaches to study the world's large river systems. *Hydrological Processes*, *27*(15), 2171–2186. https://doi.org/10.1002/hyp.9740

Luckett, L. W. (2006). Radiological conditions in areas of Kuwait with residues of depleted uranium. *Health Physics*, *90*(2), 180–181. https://doi.org/10.1097/00004032-200602000-00011

Marticorena, B., & Bergametti, G. (1995). Modeling the atmospheric dust cycle: 1. Design of a soil-derived dust emission scheme. *Journal of Geophysical Research*, *100*(D8), 16,415–16,430. https://doi.org/10.1029/95JD00690

McDiarmid, M. A., Keogh, J. P., Hooper, F. J., McPhaul, K., Squibb, K., Kane, R., et al. (2000). Health Effects of Depleted Uranium on Exposed Gulf War Veterans. *Environmental Research*, *82*(2), 168–180. https://doi.org/10.1006/enrs.1999.4012

McTainsh, G. (1980). Harmattan dust deposition in northern Nigeria. *Nature*, *286*(5773), 587–588. https://doi.org/10.1038/286587a0

National Ambient Air Quality Standards (2013). *National Ambient Air Quality Standards*. U.S.: Environmental Protection Agency, retrieved from. https://www.epa.gov/naaqs/particulate-matter-pm-air-quality-standards

Parajuli, S. P., Yang, Z.-L., & Kocurek, G. (2014). Mapping erodibility in dust source regions based on geomorphology, meteorology, and remote sensing. *Journal of Geophysical Research: Earth Surface*, *119*, 1977–1994. https://doi.org/10.1002/2014JF003095

Parajuli, S. P., Yang, Z. L., & Lawrence, D. M. (2016). Diagnostic evaluation of the Community Earth System Model in simulating mineral dust emission with insight into large-scale dust storm mobilization in the Middle East and North Africa (MENA). *Aeolian Research*, *21*, 21–35. https://doi.org/10.1016/j.aeolia.2016.02.002

Parajuli, S. P., & Zender, C. (2017). Connecting geomorphology to dust emission through high-resolution mapping of global land cover and sediment supply. *Aeolian Research*, *27*, 47–65. https://doi.org/10.1016/j.aeolia.2017.06.002

Parajuli, S. P., Zobeck, T., Kocurek, G., Yang, Z.-L., & Stenchikov, G. (2016). New insights into the wind-dust relationship from wind tunnel experiments. *Journal of Geophysical: Atmospheres*, *121*, 1776–1792. https://doi.org/10.1002/2015JD024424

Prakash, P. J., Stenchikov, G., Kalenderski, S., Osipov, S., & Bangalath, H. (2015). The impact of dust storms on the Arabian Peninsula and the Red Sea (2015). *Atmospheric Chemistry and Physics*, *15*(1), 199–222. https://doi.org/10.5194/acp-15-199-2015

Prospero, J. M., Ginoux, P., Torres, O., Nicholson, S. E., & Gill, T. E. (2002). Environmental characterization of global sources of atmospheric soil dust identified with the Nimbus 7 Total Ozone Mapping Spectrometer (TOMS) absorbing aerosol product. *Reviews of Geophysics*, *40*(1), 1002. https://doi.org/10.1029/2000RG000095

Rao, P. G., Hatwar, H. R., Al-Sulaiti, M. H., & Al-Mulla, A. H. (2003). Summer shamals over the Arabian Gulf. *Weather*, *58*(12), 471–478. https://doi.org/10.1002/wea.6080581207

Rashki, A., Kaskaoutis, D. G., Francois, P., Kosmopoulos, P. G., & Legrand, M. (2015). Dust-storm dynamics over Sistan region, Iran: Seasonality, transport characteristics and affected areas. *Aeolian Research*, *16*, 35–48. https://doi.org/10.1016/j.aeolia.2014.10.003

Reid, J. S., Reid, E. A., Walker, A., Piketh, S., Cliff, S., al Mandoos, A., et al. (2008). Dynamics of southwest Asian dust particle size characteristics with implications for global dust research. *Journal of Geophysical Research*, *113*, D14212. https://doi.org/10.1029/2007JD009752

Rinecker, M. M., Suarez, M. J., Gelaro, R., Todling, R., Bacmeister, J., Liu, E., et al. (2011). MERRA: NASA's modern-era retrospective analysis for research and applications. *Journal of Climate*, *24*(14), 3624–3648. https://doi.org/10.1175/JCLI-D-11-00015.1

Sajani, S. Z., Miglio, R., Bonasoni, P., Cristofanelli, P., Marinoni, A., Sartini, C., et al. (2011). Saharan dust and daily mortality in Emilia-Romagna (Italy). *Occupational and Environmental Medicine*, *68*(6), 446–451. https://doi.org/10.1136/oem.2010.058156

Schepanski, K., Tegen, I., Laurent, B., Heinold, B., & Macke, A. (2007). A new Saharan dust source activation frequency map derived from MSG-SEVIRI IR-channels. *Geophysical Research Letters*, *34*, L18803. https://doi.org/10.1029/2007GL030168

Schepanski, K., Tegen, I., Todd, M. C., Heinold, B., Bönisch, G., Laurent, B., & Macke, A. (2009). Meteorological processes forcing Saharan dust emission inferred from MSG-SEVIRI observations of subdaily dust source activation and numerical models. *Journal of Geophysical Research*, *114*, D10201. https://doi.org/10.1029/2008JD010325

Shao, Y. (2001). A model for mineral dust emission. *Journal of Geophysical Research*, *106*(D17), 20,239–20,254.

Shao, Y., Wyrwoll, K. H., Chappell, A., Huang, J., Lin, Z., McTainsh, G. H., et al. (2011). Dust cycle: An emerging core theme in Earth system science. *Aeolian Research*, *2*(4), 181–204. https://doi.org/10.1016/j.aeolia.2011.02.001

Sotoudeheian, S., Salim, R., & Arhami, M. (2016). Impact of Middle Eastern dust sources on PM$_{10}$ in Iran: Highlighting the impact of Tigris-Euphrates basin sources and Lake Urmia desiccation. *Journal of Geophysical Research: Atmospheres*, *121*, 14,018–14,034. https://doi.org/10.1002/2016JD025119

Su, L., & Fung, J. C. H. (2015). Sensitivities of WRF-Chem to dust emission schemes and land surface properties in simulating dust cycles during springtime over East Asia. *Journal of Geophysical Research: Atmospheres*, *120*, 11,215–11,230. https://doi.org/10.1002/2015JD023446

Taylor, K. E. (2001). Summarizing multiple aspects of model performance in a single diagram. *Journal of Geophysical Research*, *106*(D7), 7183–7192. https://doi.org/10.1029/2000JD900719

Toon, O. B., Turco, R. P., Robock, A., Bardeen, C., Oman, L., & Stenchikov, G. L. (2007). Atmospheric effects and societal consequences of regional scale nuclear conflicts and acts of individual nuclear terrorism. *Atmospheric Chemistry and Physics*, *7*(8), 1973–2002. https://doi.org/10.5194/acp-7-1973-2007

US Army Environmental Policy Institute (1995). Health and environmental consequences of depleted uranium use in the US Army, US Army Environmental Policy Institute, Technical Report, Georgia Institute of Technology, Atlanta.

Vishkaee, F. A., Flamant, C., Cuesta, J., Oolman, L., Flamant, P., & Khalesifard, H. R. (2012). Dust transport over Iraq and northwest Iran associated with winter Shamal: A case study. *Journal of Geophysical Research*, *117*, D03201. https://doi.org/10.1029/2011JD016339

Walker, A. L., Liu, M., Miller, S. D., Richardson, K. A., & Westphal, D. L. (2009). Development of a dust source database for mesoscale forecasting in southwest Asia. *Journal of Geophysical Research*, *114*, D18207. https://doi.org/10.1029/2008JD011541

White, B. R. (1979). Soil transport by winds on Mars. *Journal of Geophysical Research*, *84*, 4643–4651. https://doi.org/10.1029/JB084iB09p04643

Winker, D. M., Tackett, J. L., Getzewich, B. J., Liu, Z., Vaughan, M. A., & Rogers, R. R. (2013). The global 3-D distribution of tropospheric aerosols as characterized by CALIOP. *Atmospheric Chemistry and Physics*, *13*(6), 3345–3361. https://doi.org/10.5194/acp-13-3345-2013

Woertz, E. (2017). Food security in Iraq: results from quantitative and qualitative surveys. *Food Security*, *69*(2), 163–176. https://doi.org/10.1080/00330124.2016.1194216

Wood, W. W., Eckardt, F. D., Kraemer, T. F., & Eng, K. (2010). Quantitative Eolian Transport of Evaporite Salts from the Makgadikgadi Depression (Ntwetwe and Sua Pans) in Northeastern Botswana: Implications for Regional Ground-Water Quality. In M. Öztürk, B. Böer, H. J. Barth, M. Clüsener-Godt, M. Khan, & S. W. Breckle (Eds.), *Sabkha Ecosystems, Tasks for Vegetation Science* (Vol. 46, pp. 27–37). Dordrecht: Springer. https://doi.org/10.1007/978-90-481-9673-9_4

Wu, C., Lin, Z., He, J., Zhang, M., Liu, X., Zhang, R., & Brown, H. (2016). A process-oriented evaluation of dust emission parameterizations in CESM: Simulation of a typical severe dust storm in East Asia. *Journal of Advances in Modeling Earth Systems*, *8*, 1432–1452. https://doi.org/10.1002/2016MS000723

Zender, C. S., Bian, H., & Newman, D. (2003). Mineral Dust Entrainment and Deposition (DEAD) model: Description and 1990s dust climatology. *Journal of Geophysical Research*, *108*(D14), 4416. https://doi.org/10.1029/2002JD002775

Zender, C. S., Newman, D., & Torres, O. (2003). Spatial heterogeneity in aeolian erodibility: Uniform, topographic, geomorphic, and hydrologic hypotheses. *Journal of Geophysical Research*, *108*(D17), 4543. https://doi.org/10.1029/2002JD003039

Zhao, C., Liu, X., Leung, L. R., Johnson, B., McFarlane, S., Gustafson, W. Jr., et al. (2010). The spatial distribution of mineral dust and its shortwave radiative forcing over North Africa: Modeling sensitivities to dust emissions and aerosol size treatments. *Atmospheric Chemistry and Physics*, *10*(18), 8821–8838. https://doi.org/10.5194/acp-10-8821-2010